

**Centro de Investigación y de Estudios Avanzados
del
Instituto Politécnico Nacional**

DEPARTAMENTO DE FÍSICA

**Funciones de correlación y de estructura para
el estudio de series de tiempo no
estacionarias**

Tesis que presenta

Abraham de Jesús Aguilar Uribe

para obtener el Grado de

Maestro en Ciencias

en la Especialidad de

Física

Director de tesis: **Dr. Luis Fernando Rojas Ochoa**

Ciudad de México

Febrero, 2021



**CENTRO DE INVESTIGACION Y DE ESTUDIOS AVANZADOS
DEL INSTITUTO POLITECNICO NACIONAL**

PHYSICS DEPARTMENT

**“Correlation and structure functions for the
study of non stationary time series”**

Thesis submitted by

Abraham de Jesús Aguilar Uribe

In order to obtain the

Master of Science

degree, speciality in

Physics

Supervisor: Dr. Luis Fernando Rojas Ochoa

Mexico City

February, 2021.

Contents

List of Figures	iv
List of Tables	viii
1 Introduction	2
2 Correlation and Structure Functions	5
2.1 Stationarity and Ergodicity	6
2.2 Correlation function	6
2.3 Structure function	7
2.4 Correlation and Structure functions in their discrete form	8
2.4.1 Discrete definition of correlation and structure functions	9
2.4.2 Correlations vs Structure functions	10
2.5 Linear Correlator/Structurator and the Multi- τ algorithm	11
2.5.1 Linear Correlator/Structurator	11
2.5.2 Multi- τ Correlator/Structurator	12
2.5.3 Justification of Multi- τ for Intensity Correlations Functions	14
2.5.4 Justification of Multi- τ for structure functions	15
3 Light Scattering	18
3.1 Scattering of light	18
3.1.1 Elastic Light Scattering	20

3.1.2	Cross-correlation experiments	22
3.2	Correlation functions	22
3.2.1	Correlation function of the scattered field	23
3.2.2	Correlation function of the scattered intensity	25
3.3	Photon counts and intensity statistics	28
3.3.1	Photon statistics	29
3.3.2	Photon counts statistics	30
4	<i>PhotonSTR</i> – 18	35
4.1	About <i>PhotonSTR</i> – 18	35
4.1.1	Motivation and significance	35
4.1.2	Mathematical description	36
4.2	Software calibration	37
4.3	Time Performance	39
5	Experiments	42
5.1	Experimental setup	42
5.2	Samples	43
5.2.1	Polymer matrices of polyacrylamide	44
5.2.2	PNiPAM microgels	44
5.3	Results	44
5.3.1	Polymer matrices of polyacrylamide	45
5.3.2	PNiPAM microgel colloids	46
6	Discussion and Concluding Remarks	53
A	Calibration of the 3D LS Spectrometer	55
B	Data segmentation process	57

List of Figures

2.1	Graphical representation of a linear C/S with a lag-time $\tau = 3\Delta t$. The function $f(a_j, a_{j+3}) = a_j a_{j+3}$ for the correlation function, and $f(a_j, a_{j+3}) = (a_j - a_{j+3})^2$ for the structure function. The function Σ computes the mean value of the operations.	12
2.2	$\delta g(\tau, \Delta t)$ (left axis) for different values of $\alpha = \tau/\Delta t$ and $\delta g(0, \Delta t)$ (right axis) as a function of $\Delta t/\Gamma$. The dotted line represents the upper bound 10^{-3} , and it is used in the left axis. The plots for $\alpha \leq 7$ may cross the upper bound 10^{-3} while for $\alpha \geq 7$ these never crosses the upper bound regardless of the value $\Delta t/\Gamma$. The plot for $\delta g(0, \Delta t)$ shows how the function has a lower bound of 10^0	16
3.1	Representation of a light scattering experiment. A light beam with intensity I_o and with a wave-vector \vec{k}_o impinges over a volume of the sample. The sample consists of scatterers immersed in a continuous media. The transmitted light is not of interest since it did not interacted with the sample. The scattered light beam is collected at an angle θ , measured with respect to the transmitted beam. The detector used for <i>SLS</i> can be a light intensity detector while for <i>DLS</i> it must be a photon detector.	20

- 3.2 Representation of a cross-correlation experiment. A light beam is splitted by a beam splitter (BS). The two beams are directed to the sample by a mirror (M) and a lens (L) and they impinge over the same volume, then the two scattered beams are detected by two different detectors (D1 and D2) at the same scattered angle θ 23
- 3.3 Representation of $I_s(t, \vec{q})$ (red line), the photon events (yellow bars) and n_j (green bars). n_j is a discrete function of width Δt . The height of n_j is determined by the number of photon events within its width, for example n_1 is equal to two units, n_2 is equal to one unit and so on. 29
- 3.4 Plot of $\overline{W}\mathbb{P}(W/\overline{W})$ for polarized thermal light (blue continuous line). Plots of the distribution of photon counts $\mathcal{P}(k)$ are presented with $\bar{k} = 1$ (green squares) and $\bar{k} = 0.5$ (red circles). The points are joined by a dashed line but only the integer values of k makes sense. It can be seen that the exponential decay of $\overline{W}\mathbb{P}(W/\overline{W})$ is somehow preserved for $\mathcal{P}(k)$ 31
- 3.5 Plot of $\overline{W}^2\mathbb{P}(W/\overline{W})$ for unpolarized thermal light (red continue line plotted in the right axis). Plots of the distribution of photon counts $\mathcal{P}(k)$ are presented with $\bar{k} = 1$ (blue circles) and $\bar{k} = 4$ (green squares). The form of $\overline{W}^2\mathbb{P}(W/\overline{W})$ is not preserved by $\mathcal{P}(k)$. For $\bar{k} = 1$ $\mathcal{P}(k)$ is a decreasing function, while for $\bar{k} = 4$ it increases and decreases. The two lines meet at $\bar{k} = 2$ 33
- 3.6 Plot of $\overline{W}\mathbb{P}(W/\overline{W})$ using the left y axis for different values of $\mathcal{P} = 0.9$ (black solid line), $\mathcal{P} = 0.6$ (red solid line) and $\mathcal{P} = 0.3$ (blue solid line). The graphs of $\mathcal{P}(k)$ are represented by squares for $\mathcal{P} = 0.9$, triangles for $\mathcal{P} = 0.6$ and circles for $\mathcal{P} = 0.3$. The dashed lines corresponds to $\bar{k} = 1$, while the dotted lines are for $\bar{k} = 4$. The form of $\overline{W}\mathbb{P}(W/\overline{W})$ may not be preserved by $\mathcal{P}(k)$. . 34
- 4.1 Plot of the ICF and ISF functions for the two channels A and B and for the cross-structure function AxB . The continuous lines correspond to the fits. . 38

4.2	Time performance of the three different programs. We used the notation $Mp = x, m = y$ and $Lp = x, m = y$ for Matlab and Labview respectively, with $x = 16, 32, 64$ and $y = 2, 4$. We do not present any result of a run taking more than 3 hours.	40
5.1	3D LS Spectrometer set-up. The laser light first enter to the Deflection unit to be directed to a beam splitter. Then, the light is split in two beams and directed to the sample by the lens L_1 . The sample is kept in the Cell housing unit, where it is maintained at a fixed temperature by the thermal bath. The scattered photons are directed to the lens L_2 and then to the Detection unit, where they are collected and recorded by the detectors channels A and B. The Detection unit is assembled with the Goniometer by an arm. The optical alignment is such that any effect due to light refraction of light is compensated in the thermal bath.	43
5.2	($IACF$ & $IASF$) functions for the four different samples. Continuous lines are the fitting results.	45
5.3	Principal peak of the static scattered intensity of the sample $C5$ (left) and the principal peak with a higher angular resolution (right).	47
5.4	Intensity cross-correlation functions of four different measurements.	48
5.5	Intensity cross-structure functions of four different measurements.	49
5.6	Photon counts of the different measurements. The first plot corresponds to the measurement 1, the second to the 2 and so on. In the four graphs, the blue curve refers to the detector channel A and the red one to channel B. We can observe how the mean value of the time series is changing, which is a signature of a non-stationary process.	50
5.7	Probability density function $\mathcal{P}(k)$ of the four measurements. Only values from $k = 0$ to $k = 10$ are shown, higher values have almost zero probability. In general, we see a good agreement between the data and the fits.	51

A.1	Intercept $g^{(2)}(\tau \rightarrow 0)$ (left y axis) and $\langle I_s \rangle$ (right y axis). The continuous line corresponds to the fit with the model described in the text.	56
-----	--	----

List of Tables

4.1	Estimated radius in the calibration process.	39
5.1	Values of γ and τ_o obtained in the fitting process using the model <i>IACF</i> & <i>IASF</i> . 46	
5.2	Values of the parameters \mathcal{P} and \bar{k} of the four measurements for both detector channels A and B. M1 stands for measurement 1 and so on.	52

Abstract

Correlation and structure functions are widely used in many branches of physics and in general in stochastic analysis. Correlation functions are well supported by many theoretical and technical works treating its fast calculations and statistical accuracy. The structure-function has received less attention than the correlation function, but it offers a better performance in some analysis, and it is the only function capable of characterizing nonstationary process with unitary increments.

In this thesis, we present *PhotonSTR* – 18, a free LabVIEW software. This software computes the auto and cross-correlation and structure-functions in an off-line mode in parallel. To do so, we extended the multi- τ algorithm, initially formulated for calculating the correlation function, to calculate the structure-function. The algorithm allows the fast calculation of the structure-function by software. These two functions, correlation and structure functions, are used to analyze phenomena where there is a fluctuation in the intensity of events over time, as in chemical, biological, and other physical processes.

To show the use of *PhotonSTR* – 18, we perform light scattering experiments using polyacrylamide networks and PNIPAM microgel colloidal systems as samples. In our experiment, we avoid using a hardware correlator; instead, we save the photon history of the scattered photons and use *PhotonSTR* – 18 to perform the analysis. Using our software, we obtain the advantage of having both the correlation and the structure-function without losing the photon history. We pay special attention to the results of the binary-charged colloidal suspensions due to unexpected results. This system's cross-correlation function passes from

being a decreasing function to an increasing function as time evolves. We use the photon history to make a more in-depth analysis of the time series.

Resumen

Las funciones de correlación y de estructura son ampliamente usadas en muchas áreas de la física y en general en el análisis estocástico. Las funciones de correlación están bien fundamentadas por muchos trabajos tanto teóricos como prácticos donde se aborda su cómputo rápido y su exactitud estadística. Por su parte, la función de estructura ha recibido menos atención y uso que la función de correlación, sin embargo, esta ofrece un mejor desempeño en algunas situaciones y es la única capaz de caracterizar procesos no estacionarios con incrementos unitarios.

En esta tesis presentamos *PhotonSTR* – 18, un software libre programado en LabView. Este software realiza el cómputo en paralelo de las funciones de correlación y de estructura en modo auto y cross- de manera ”off-line”. En este contexto, se extendió el algoritmo Multi- τ , originalmente formulado para las funciones de correlación, para calcular las funciones de estructura lo cual permite el cómputo rápido de las funciones de estructura por software. Ambas funciones pueden ser utilizadas para analizar fenómenos donde existe una fluctuación en el tiempo de alguna señal, tal y como sucede en química, biología y algunos procesos físicos.

Para mostrar el uso de *PhotonSTR* – 18 realizamos experimentos de dispersión de luz usando como muestras redes de polyacrylamide y microgeles coloidales de PNiPAM. En los experimentos se evita el uso de correladores por hardware, en su lugar, se guardó el tiempo de llegada de los fotones dispersados y se usó *PhotonSTR* – 18 para realizar el análisis. Esto nos da la ventaja de tener no solamente la función de correlación sino también la función

de estructura y sin perder el registro de los tiempos de llegada de los fotones. Se presta atención especial a los resultados de los cristales binarios de partículas de Latex debido a unos resultados inesperados. Las funciones de cross-correlación pasan de ser funciones decrecientes a ser crecientes con el paso del tiempo. Usamos el tiempo de llegada de los fotones para hacer un análisis más profundo de los resultados.

Acknowledgements

Quiero dedicar esta tesis a mis padres y hermanos por todo su apoyo durante mis estudios. Este logro no hubiera sido posible sin ellos. Quiero agradecer a mis compañeros y amigos que hicieron de mi maestría una experiencia inolvidable. Especialmente quiero agradecer a Lilibeth por todo su apoyo y ánimos durante mi trabajo de tesis.

También quiero agradecer al Dr. Luis Fernando Rojas Ochoa por su tutoría y su apoyo, y a todo el equipo de trabajo del laboratorio T18 por su apoyo.

Finalmente, quiero agradecer a CONACyT por la beca 935775 que me permitió llevar a cabo mis estudios de maestría y al Cinvestav por su apoyo brindado.

Chapter 1

Introduction

Correlation functions (CF) are widely used in condensed matter and quantum optics experiments. For example, in the field of the so-called photon correlation spectroscopy, CF are used to determine the diffusion coefficient of colloidal particles in suspension and their size distribution [1]. The interesting phenomena of glass transition [2, 3] is studied in terms of CF among other examples [4]. The use of CF is well supported by many theoretical works, analyzing its statistical accuracy; and technical works (see for example [1, 5, 6, 7, 8]). In particular, we highlight the Multi- τ algorithm which is critical for a fast calculation of the CF . This algorithm reduces drastically the total number of operations required to compute the CF . The fast calculation of CF by software and the online calculation by hardware makes the CF an excellent option to be used in condensed matter experiments.

The structure-function (SF), first proposed by Kolmogorov in fluid mechanics, is also defined on the same grounds as the CF . Historically, the SF has received less attention than the CF . There are only a few theoretical works [1, 5, 9, 10] and none experimental technical work regarding the use of SF despite the fact it is less sensitive to statistical errors. To our knowledge, there is not a single paper in literature treating the fast calculation of the SF . We believe this is one of the reasons why the use of structure-function in photon correlation spectroscopy has been almost ignored.

Both CF and SF are equivalent when characterizing wide-sense stationary processes. A more general kind of processes are the non-stationary processes with stationary increments [11], where we can not use correlation functions and the structure functions are the only possible choice [9, 1]. In the general case, a time series is not necessarily wide-sense stationary. The use of the correlation function alone is risky in these cases since it may not characterize the process adequately. Thus, a fast calculation of both correlation and structure (CF & SF) functions is desired. Additionally, (CF & SF) functions have different statistical properties, and even in the case of a wide sense stationary process, one could be more accurate than the other.

Here we extend the use of the Multi- τ algorithm, initially designed to calculate the correlation-function, to make the fast calculation of the structure-function possible. We present *PhotonSTR*—18 [12], a LabView free software that computes the auto and cross- (CF & SF) functions in parallel by the multi- τ algorithm in offline mode. The theory behind *PhotonSTR*—18 is displayed in this work together with a time performance analysis of our software. We consider that the software architecture presented here can be exported to other language programs and even hardware.

To test our mathematical model and software, we perform light scattering experiments. We use a 3D LS spectrometer (LS Instruments AG, Switzerland) working with a He-Ne laser and two avalanche photodiodes as detectors. The configuration of the 3D LS device allows us to perform two scattering experiments simultaneously on the same scattering volume; thus, obtaining the photon history of the two scattered beams and therefore being able to compute auto and cross (CF & SF) functions. In our scattering experiments, we choose stationary and non-stationary systems to show the structure-function's advantages over the correlation function. The systems used are turbid media, known for being non-stationary systems as the media becomes more turbid.

One of the systems under study are polymer matrices of polyacrylamide (PA), as those used in reference [13]. We choose these systems because they are Polyacrylamide gels whose

elasticity depends linearly on the amount of cross-linking f_{Bis} for small concentrations of bisacrylamide [13]. We should expect light scattering from such systems departs from a pure wide-sense stationary random process as f_{Bis} grows and the system becomes a non-stationary process.

The second system under study is a binary charged colloidal suspension at low ionic strength, composed of latex particles of different sizes suspended in deionized water. We pay special attention to the results obtained from this system, because the correlation function pass to be a decreasing function ($g^{(2)}(\tau) > g^{(2)}(\tau + \delta\tau)$) to a increasing function ($g^{(2)}(\tau) < g^{(2)}(\tau + \delta\tau)$). A similar behaviour is found in the the structure-function.

The thesis is organized as follows. Chapter 2 displays the definition of the correlation and structure function in their continuous and discrete forms together with a brief discussion of their statistical properties. Later the Multi- τ algorithm for the correlation function is presented, then we show how to compute the structure-function with the Multi- τ algorithm. Chapter 3 reviews light scattering and derive the correlation and structure functions of the scattered intensity, and discusses their equivalence to the photon counts' correlation and structure functions. Additionally, we derive the photon counts' probability density functions for different cases of the detected light. In chapter 4 we present *PhotonSTR* – 18. We give a short mathematical description, a calibration, and a time performance analysis of our software. In chapter 5, we describe our experimental setup and the synthesis of the samples. The results of our experiments are shown together with an analysis of the results. Last, in chapter 6, we present some concluding remarks of the work presented in this thesis.

Chapter 2

Correlation and Structure Functions

We begin this chapter introducing some concepts of the theory of random processes, the intention is to be self consistent rather than give a complete background. A random process $A(t)$ is a mathematical concept which includes all possible outcomes of an experiment $\{a_1(t), a_2(t), \dots\}$, where each function $a(t)$ represents a particular outcome of an experiment and t is the time or a evolution parameter. We will refer to $a(t)$ as sample function and to the complete set of sample functions as the ensemble of such functions. One may think of the sample function $a(t)$ as the outcome of a detector. The necessity of the definition of the random process lies in the fact that in experiments where the sample function $a(t)$ is a measure over time, it is unlikely that if we repeat the experiment we measure the exact same $a(t)$, instead we measure another sample function of the ensemble of functions, say $b(t)$. Nonetheless, the two sample functions $a(t)$ and $b(t)$ may be different but they may hold similar or same information of the experiment. Thus, we need a mathematical background to deal whit these functions. In this chapter, we first introduce the concept of stationarity and ergodicity of a random process. Then, the definitions of the correlation and structure functions are presented and finally the Multi-Tau algorithm is introduced.

2.1 Stationarity and Ergodicity

In the theory of random processes we say that a random process $A(t)$ is *Wide-Sense Stationary* (WSS) if the following conditions are met [11]: the expected value $E[a(t)]$ is independent of t and $E[a(t_1)b(t_2)]$ depends only on $\tau = t_1 - t_2$, being $a(t)$ and $b(t)$ two sample functions of the random process $A(t)$. From these two conditions one concludes that in a *WSS* process, the statistical properties does not depend on the time origin. Another concept necessary for our study is *Ergodicity*, which in the language of random processes consists in the equivalence between temporal and ensemble averages[14].

2.2 Correlation function

The correlation function G is defined as [11],

$$G_{ab}(\tau) = \lim_{T \rightarrow \infty} \frac{1}{T} \int_0^T a(t + \tau)b(t)dt = \langle a(t + \tau)b(t) \rangle, \quad (2.1)$$

where $\langle \rangle$ indicates temporal average, a and b are two sample function of a stochastic process and τ is the lag time. Usually, if $a(t) = b(t)$ then $G_{aa}(\tau)$ is called auto-correlation function, otherwise, its called cross-correlation function. The correlation function can be understood as the average of the similarity of the function $a(t)$ and $b(t)$. Additionally, the statistical correlation function is defined as;

$$\bar{G}_{ab}(t_1, t_2) = \int_{-\infty}^{\infty} \int_{-\infty}^{\infty} a(t_1)b(t_2)P(a, b; t_1, t_2)dadb = \overline{a(t_1)b(t_2)} \quad (2.2)$$

where $a(t_1)$ and $b(t_2)$ are the sample functions at time t_1 and t_2 , respectively, $P(a, b; t_1, t_2)$ is the join probability density function of the sample functions $a(t_1)$ and $b(t_2)$ and $\overline{a(t_1)b(t_2)}$ indicates ensemble average. For an ergodic process, $G_{ab}(\tau) = \bar{G}_{ab}(t_1, t_2)$ with the condition that $\tau = t_1 - t_2$. In practice, one computes the correlation function and not the statistical correlation function due the difficulty to specify $P(a, b; t_1, t_2)$. From equation 2.1, limit cases

and properties of $G_{ab}(\tau)$ can be computed, these are [11]:

$$G_{ab}(0) = \langle a(t)b(t) \rangle, \quad (2.3)$$

$$G_{ab}(\tau) = G_{ab}(-\tau), \quad (2.4)$$

$$\sqrt{G_{aa}(0)G_{bb}(0)} \geq |G_{ab}(\tau)|. \quad (2.5)$$

In the literature is common to use the normalized correlation function $g(\tau)$ instead of $G(\tau)$, defined as

$$g_{ab}(\tau) = \frac{G_{ab}(\tau)}{\langle a \rangle \langle b \rangle}, \quad (2.6)$$

where we assume stationarity for the mean values of the sample functions, $a(t)$ and $b(t)$.

2.3 Structure function

The structure function is defined as [11]

$$S_{ab}(\tau) = \lim_{T \rightarrow \infty} \frac{1}{T} \int_0^T (a(t+\tau) - b(t))^2 dt = \langle (a(t+\tau) - b(t))^2 \rangle. \quad (2.7)$$

Again, if $a(t) = b(t)$ then $S_{aa}(\tau)$ is called auto-structure function, otherwise, it is called cross-structure function. As well as the correlation function, the statistical structure function is defined as

$$\bar{S}_{ab}(t_1, t_2) = \int_{-\infty}^{\infty} \int_{-\infty}^{\infty} (a(t_1) - b(t_2))^2 P(a, b; t_1, t_2) da db = \overline{(a(t_1) - b(t_2))^2}. \quad (2.8)$$

For ergodic processes $S_{ab}(\tau) = \bar{S}_{ab}(t_1, t_2)$ with the condition $\tau = t_1 - t_2$. The structure function can be cast in analogy to the mean square displacement. Again, due to the impossibility of specifying $P(a, b; t_1, t_2)$, one computes the structure function and not the statistical

structure function. The structure and the correlation function are related by the equality

$$S_{ab}(\tau) = \langle a(t + \tau)^2 \rangle + \langle b(t)^2 \rangle - 2G_{ab}(\tau). \quad (2.9)$$

For a *WSS* process, Equation 2.9 turns into

$$S_{ab}(\tau) = G_{aa}(0) + G_{bb}(0) - 2G_{ab}(\tau). \quad (2.10)$$

As the correlation function, the structure function can also be expressed in its normalized form, which definition is

$$s_{ab}(\tau) = \frac{S_{ab}(\tau)}{2\langle a \rangle \langle b \rangle}. \quad (2.11)$$

2.4 Correlation and Structure functions in their discrete form

The definitions of the correlation and structure functions C & S need an explicit form of the sample functions $a(t)$ and $b(t)$ in order to be calculated. On the other hand, in an experiment only the discrete and finite forms of these function are available, in consequence, discrete forms of equations 2.1 and 2.7 are needed. The discrete form of a sample function a_j , $j = 0, 1, \dots, T$, where T is an integer, is a set of $T + 1$ numbers. Experimentally, the sample functions are the result of a segmentation process (see appendix B). The raw data of a detector is averaged over time intervals of width Δt . We will refer to Δt as the sample time. As an example, in DLS each a_j represent the sum of photons detected in the j th time window of width Δt and it is a discrete version of the number of detected photons per unit of time. We also present the C & S functions in they normalized form. Additionally, definitions of the moments of the sample functions are presented.

2.4.1 Discrete definition of correlation and structure functions

The discrete definitions of the correlation and structure functions are [9]

$$\hat{G}_{ab}(\tau) = \frac{1}{T - \tau} \sum_{i=0}^{T-\tau-1} a_{i+\tau} b_i = \langle a_{i+\tau} b_i \rangle, \quad (2.12)$$

$$\hat{S}_{ab}(\tau) = \frac{1}{T - \tau} \sum_{i=0}^{T-\tau-1} (a_{i+\tau} - b_i)^2 = \langle (a_{i+\tau} - b_i)^2 \rangle, \quad (2.13)$$

where τ is the discrete lag time $\tau = 0, \Delta t, \dots, T\Delta t$ and the hat stands for estimator. One should note that the number of terms decreases as τ increases, thus, $\hat{G}_{ab}(\tau)$ and $\hat{S}_{ab}(\tau)$ decrease in statistical accuracy as τ increase. A relation between $\hat{G}_{ab}(\tau)$ and $\hat{S}_{ab}(\tau)$ is also present in their discrete form

$$\hat{S}_{ab}(\tau) = \frac{1}{T - \tau} \sum_{i=1}^{T-\tau} (a_{i+\tau}^2 + b_i^2) - 2\hat{G}_{ab}(\tau) = \langle a^2 \rangle_{i+\tau} + \langle b^2 \rangle_i - 2\hat{G}_{ab}. \quad (2.14)$$

Where terms of the type $\langle a^2 \rangle_{i+\tau}$ are given by

$$\langle a^2 \rangle_{i+\tau} = \frac{1}{T - \tau} \sum_{i=1}^{T-\tau} a_{i+\tau}^2. \quad (2.15)$$

For a *WSS* process $\hat{G}_{ab}(\tau)$ and $\hat{S}_{ab}(\tau)$ are related by

$$\hat{S}_{ab}(\tau) = \hat{G}_{aa}(0) + \hat{G}_{bb}(0) - 2\hat{G}_{ab}(\tau). \quad (2.16)$$

The moments of the discrete samples functions can be easily computed, the first moment of a sample function for a *WSS* process is

$$\langle a \rangle = \frac{1}{T} \sum_{i=0}^{T-1} a_i, \quad (2.17)$$

the second moment of the sample function is

$$\langle a^2 \rangle = \frac{1}{T} \sum_{i=0}^{T-1} a_i^2. \quad (2.18)$$

Higher order moments are computed similarly. As it was mentioned, the discrete estimators do not include any consideration of possible noise in the data; then, we introduce the following estimators for the correlation and structure functions, respectively

$$\hat{g}_{ab}^{(2)}(\tau) = \frac{\hat{G}_{ab}(\tau)}{\langle a \rangle \langle b \rangle} - 1 = \hat{g}_{ab}(\tau) - 1 \quad (2.19)$$

and

$$\hat{s}_{ab}^{(2)} = \frac{\hat{S}_{ab}}{2\langle a \rangle \langle b \rangle}, \quad (2.20)$$

These estimators reduce the estimator's noise [6, 10], and are used in this work.

2.4.2 Correlations vs Structure functions

Even though the definitions of the correlation and structure functions are similar, they have different statistical properties. The signal to noise ratio (S/N) behaves differently for each functions, it depends on the nature of the noise in the data. The structure function is less sensitive to low frequency noise [9], which leads to a better (S/N) ratio for short lag times as compared with the correlation function. In photon detection experiments, the high frequency noise is dominated by the low frequency noise for which the correlation function is less sensitive [5].

In the context of DLS, the length of the measured data, the sample time of the raw data and photon count rate also affects the accuracy of the estimators. For high photon count rate $\langle a \rangle / \gamma \geq 1$, there is a region of lag times $\tau < \Delta t / \tau_c = \gamma$; with τ_c being the coherence time, where the structure function shows less statistical error than the correlation function [5]. Increasing the ratio $\langle a \rangle / \gamma$ expands this region of lag times. On the contrary, for larger lag times, the correlation function presents less statistical error. For short data length $T < 10^4$,

the structure function shows less error than the correlation function for $\langle a \rangle \geq 1$ and short lag times [5].

2.5 Linear Correlator/Structurator and the Multi- τ algorithm

In order to compute the correlation and structure functions in their discrete form, one can make use of a linear Correlator/Structurator (C/S), which computes the structure and correlation function using their discrete definition. Using a linear C/S could be computationally expensive, for example; in a data set of $T + 1 \gg 1$ numbers, a_j $j = 0, \dots, T$ in order to compute C & S functions at all lag times $0 \leq \tau \leq T$, approximately T^2 operations are required. On the other hand, a Multi- τ algorithm can compute the correlation and structure functions in a fraction of a time compared to a linear correlator. The multi- τ algorithm uses an ensemble of K linear C/S , each one of them computes the correlation and structure functions increasing the sample time semi-logarithmically, in the segmentation process of the data. Theoretical justification for Multi- τ algorithm is presented for both C & S , we first present the one for correlation function and then we show how this can be extended to structure functions.

2.5.1 Linear Correlator/Structurator

The architecture of a linear C/S consists of P counters, each one of them computes the correlation and structure function at a different value of τ . For example, the channel $P = 0$ computes the C & S functions at lag-time $\tau = 0$, the counter $P = 1$ computes at lag-time $\tau = 1$ and so on. The linear C/S covers the lag times $0 \leq \tau \leq P\Delta t$, a illustrative picture of a linear C/S is presented in figure 2.1. The selection of the number P must be done considering that the length of the time series used in the last counter is long enough to

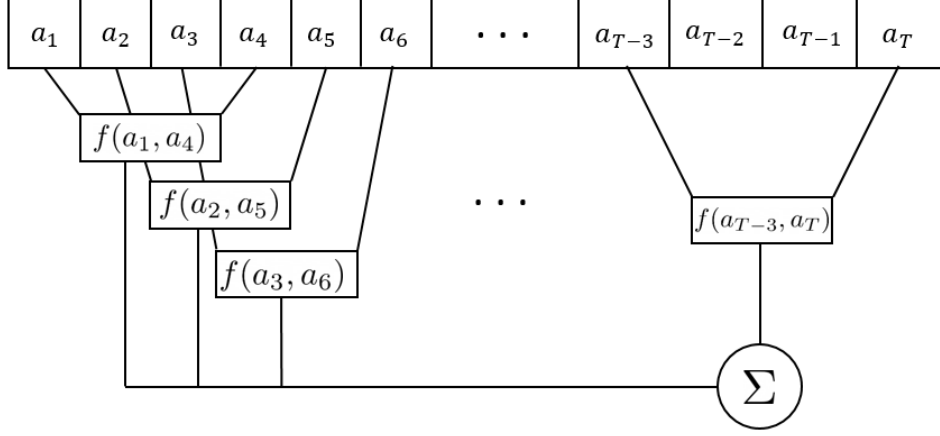


Figure 2.1: Graphical representation of a linear C/S with a lag-time $\tau = 3\Delta t$. The function $f(a_j, a_{j+3}) = a_j a_{j+3}$ for the correlation function, and $f(a_j, a_{j+3}) = (a_j - a_{j+3})^2$ for the structure function. The function Σ computes the mean value of the operations.

reduce the statistical errors. The number of operations to compute C & S functions at $P = cT$ lag times, where $0 \leq c \leq 1$ is a constant, in a data set of $T \gg 1$ is approximately $PT = cT^2$. Different schemes of linear C/S have been reported in the literature[8, 15].

2.5.2 Multi- τ Correlator/Structurator

The multi- τ algorithm consists of an ensemble of K linear C/S with P counters and each one of them increases the lag-time logarithmically. The sample time of the l th, $l = 0, \dots, K$ C/S order scales as $\Delta t_l = m^l \Delta t_0$, where Δt_0 is the sample time of the 0th C/S and $m \geq 2$ is an integer. In consequence, the l th C/S covers lag times $\tau = 0, m^l \Delta t_0, \dots, m^l P \Delta t_0$ and it computes the discrete estimator of the C & S with less operations than a linear C/S . Approximately $PTm/(m-1)$ operations are needed to compute C & S functions. In the multi- τ algorithm typically P is at most 256 and m is at most 4. Finally, the C & S functions are obtained by properly joining the channels of C & S functions calculated in each correlator.

To illustrate this better we introduced the following notation; let $\hat{G}^{(l)}(\tau)$, $\hat{S}^{(l)}(\tau)$, $a_j^{(l)}$ and $b_j^{(l)}$ be the estimators of the C & S functions and the j th numbers in the data sets in the

l th linear C/S . We stress that the lag time scales different in each C/S , in the $l - th$ C/S $\tau = 0, \dots, m^l P \Delta t_0$ in steps of $m^l \Delta t_0$. Thus, the definitions of the normalized discrete estimator of the C & S functions in the context of multi- τ algorithm become

$$\hat{g}_{ab}^{(l)}(\tau) = \frac{1}{T_l - \tau} \sum_{i=0}^{T_l - \tau - 1} \frac{a_{i+\tau}^{(k)} b_i^{(k)}}{\langle a \rangle \langle b \rangle}, \quad (2.21)$$

$$\hat{s}_{ab}^{(l)}(\tau) = \frac{1}{T_l - \tau} \sum_{i=0}^{T_l - \tau - 1} \frac{(a_{i+\tau}^{(l)} - b_i^{(l)})^2}{2\langle a \rangle \langle b \rangle} = \frac{\langle (a^{(l)})^2 \rangle_{i+\tau} + \langle (b^{(l)})^2 \rangle_i - 2\hat{G}_{ab}^{(l)}(\tau)}{2\langle a \rangle \langle b \rangle}. \quad (2.22)$$

Where the mean values of the sample functions are computed at $l = 0$, $T_l = T/m^l$. For a WSS process, the terms $\langle (a^{(l)})^2 \rangle_{i+\tau}$ and $\langle (b^{(l)})^2 \rangle_i$ are reduced to $G_{aa}^{(l)}(0)$ and $G_{bb}^{(l)}(0)$. We want to emphasize that the length of the data set is reduced since $T_l \leq T$. Not all lag times computed in the C/S for $k \geq 1$ are useful since some times overlap.

Increasing the sample time introduces systematic errors [7, 8]. The values of the C & S functions calculated with different sample time but with the same lag-time do not necessarily match, for example, $g^{(1)}(\tau = 1) \neq g^{(0)}(\tau = 2)$ with $m = 2$. These systematic errors can be set to be in the order of 10^{-3} or less (less than unavoidable errors [5, 6, 10]) if we choose $P/m \geq 8$ and join the C & S properly. To join the counters of the C & S functions calculated in the different C/S we use all lag times with $l = 0$. Then, these are joined with the channels at $l = 1$ and $\tau > P/m \Delta t_0$ to avoid overlapping, the next ones are joined in the same way,

$$\hat{g}(\tau) = \hat{g}^{(0)}(\tau) \cup \hat{g}^{(1)}(\tau > P/m) \cup \dots \cup \hat{g}^{(K)}(\tau > P/m) \quad (2.23)$$

$$\hat{s}(\tau) = \hat{s}^{(0)}(\tau) \cup \hat{s}^{(1)}(\tau > P/m) \cup \dots \cup \hat{s}^{(K)}(\tau > P/m). \quad (2.24)$$

The systematic error introduced by increasing the sample time behaves differently in each function. In the correlation function the systematic error is 10^{-3} in average [6, 7], thus, it does not present substantial distortions. This is totally different for the structure functions,

the use of equation 2.22 introduces systematic errors, at less, in the order of 10^0 , which are much larger than any other possible error and leads to substantial distortions. The source of this errors are the therms $\langle (a^{(l)})^2 \rangle_{i+\tau}$ and $\langle (b^{(l)})^2 \rangle_i$, which have a huge systematic error while $\hat{G}_{ab}^{(l)}(\tau)$ holds an average error of 10^{-3} . The solution to this problem is to use $\langle (a^{(0)})^2 \rangle_{i+\tau}$ and $\langle (b^{(0)})^2 \rangle_i$ instead of $\langle (a^{(l)})^2 \rangle_{i+\tau}$ and $\langle (b^{(l)})^2 \rangle_i$ in equation 2.22; by doing this, we reduce the systematic error to the one introduced by $G_{ab}^{(l)}(\tau)$. Additionally, the terms $\langle (a^{(0)})^2 \rangle_{i+\tau}$ and $\langle (b^{(0)})^2 \rangle_i$ present shot noise and must be properly corrected. Shot noise naturally appears in photon detection process, it is due to the discrete nature of light and electric current and it can be shown than only the terms of the type $\tau = 0$ suffers from it [15]. This type of noise also appears in the auto-correlation function $G_{aa}^{(0)}(0)$ must be corrected as well.

2.5.3 Justification of Multi- τ for Intensity Correlations Functions

The estimation of a discrete correlation function depends non-trivially in the sample time, choosing different sample times leads to different correlations functions. Nevertheless, the gap between correlation functions computed with different sample time can be tuned to minimize the associated errors. To show this we consider the well known relationship between the expectation value of the estimator of the intensity correlation function and the theoretical intensity correlation function[6],

$$\langle \hat{g}(\tau) \rangle_{TA} = \frac{1}{(\Delta t)^2} \int_{-\Delta t}^{\Delta t} \frac{\langle I(t)I(t+\tau) \rangle}{\langle I(0) \rangle^2} (\Delta t - |t|) dt = \frac{1}{(\Delta t)^2} \int_{-\Delta t}^{\Delta t} g(\tau) (\Delta t - |t|) dt \quad (2.25)$$

where Δt is the sample time, $\langle I(0) \rangle^2$ is a normalization factor and $\langle \rangle_{TA}$ stands for triangular average. It is important to understand equation 2.25, first, the estimator $\langle \hat{g}(\tau) \rangle_{TA}$ is a smoothed version of the intensity correlation function $g(\tau)$. Second, the chose of the sample-time can lead to distortions on the estimator due the fluctuation of $g(\tau)$. Third, equation 2.25 holds for auto-correlation functions and cross-correlation functions.

If an algebraic form of $g(\tau)$ is known, the gap $\delta g = \langle \hat{g}(\tau) \rangle_{TA} - g(\tau)$ can be calculated. This gap depends on the sample time Δt as well as the lag-time τ . The gap represents the systematic error due to the triangular average and is required to be as small as possible. An relevant case is when $g(\tau) = 1 + \exp(-2\tau/\Gamma)$ (diffusive motion of colloids in suspension), where Γ is a constant. A simple calculation leads to [7],

$$\delta g(\tau, \Delta t) = e^{-2\tau/\Gamma} \left\{ \left(\frac{\sinh(\Delta t/\Gamma)}{\Delta t/\Gamma} \right)^2 - 1 \right\}, \quad (2.26)$$

this formula is valid only for the case $\tau \geq \Delta t$. When $0 \leq \tau \leq \Delta t$ the gap δg is

$$\delta g(\tau, \Delta t) = \frac{1}{(2\Delta t/\Gamma)^2} \left\{ e^{-2(\Delta t/\Gamma - \tau)} + e^{-2(\Delta t/\Gamma + \tau)} + 4(\Delta t/\Gamma - \tau/\Gamma) \right\} - \frac{1}{2} e^{-2\tau/\Gamma} \left(\frac{1}{(\Delta t/\Gamma)^2} - 2 \right), \quad (2.27)$$

it is easy to show that equations 2.26 and 2.27 match in the case $\tau = \Delta t$. Equation 2.27 can be deduced from the results of reference [8].

A graphical representation of equations 2.26 and 2.27 is presented in figure 2.2. As we see in figure 2.2, the upper bound of $\delta g(\tau, \Delta t)$, with $\tau \geq \Delta t$, tends to 0 as the $\alpha = \tau/\Delta t$ grows. Therefore, we are able to choose the maximum value of $\delta g(\tau, \Delta t)$ by tuning τ and Δt . If we wish to assure a maximum error of 10^{-3} between each merge of the correlation function in the multi- τ algorithm, we must set $\tau/\Delta t \geq 8$. In the multi- τ algorithm, this condition is achievable by setting $P/m \geq 8$, and this guaranties a maximum systematic error of 10^{-3} between each joint in the multi- τ algorithm.

2.5.4 Justification of Multi- τ for structure functions

Following the same philosophy of the subsection above, we calculated the gap $\delta s = \langle \hat{s}(\tau) \rangle_{TA} - s(\tau)$; where, for the sake of simplicity, we used the auto-structure function but these results hold for cross-structure function as well. For a wide sense stationary process δs is

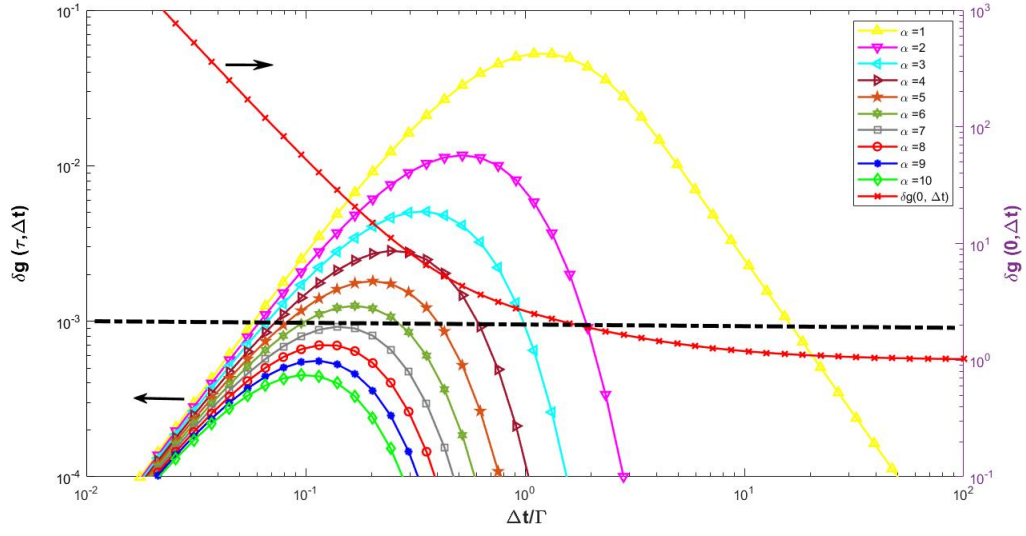


Figure 2.2: $\delta g(\tau, \Delta t)$ (left axis) for different values of $\alpha = \tau/\Delta t$ and $\delta g(0, \Delta t)$ (right axis) as a function of $\Delta t/\Gamma$. The dotted line represents the upper bound 10^{-3} , and it is used in the left axis. The plots for $\alpha \leq 7$ may cross the upper bound 10^{-3} while for $\alpha \geq 7$ these never crosses the upper bound regardless of the value $\Delta t/\Gamma$. The plot for $\delta g(0, \Delta t)$ shows how the function has a lower bound of 10^0 .

$$\delta s(\tau, \Delta t) = 2\delta g(0, \Delta t) - 2\delta g(\tau, \Delta t). \quad (2.28)$$

We have already discussed the term $\delta g(\tau, \Delta t)$, and we concluded that the error can be set to be smaller than 10^{-3} by fixing the parameters P and m . The term $\delta g(0, \Delta t)$ is more complicated to treat since it only depends on Δt and, as it can be seen in figure 2.2, it has a lower bound of 10^0 . Therefore, to avoid the introduction of systematic errors we have changed the terms $G_{aa}^{(l)}(0)$ and $G_{bb}^{(l)}(0)$ by $G_{aa}^{(0)}(0)$ and $G_{bb}^{(0)}(0)$.

We generalized this result for terms of the type $\langle (a^{(l)})^2 \rangle_i$ alike to $G_{aa}^{(l)}(0)$, and assume that they also have a big systematic error. This suggests the use of terms of the type $\langle (a^{(0)})^2 \rangle_i$ instead of $\langle (a^{(l)})^2 \rangle_i$ to construct the structure function. In consequence, equation 2.22 is changed by the following equation

$$\hat{s}_{ab}^{(l)}(\tau) = \frac{\langle (a^{(0)})^2 \rangle_{i+\tau} + \langle (b^{(0)})^2 \rangle_i - 2\hat{G}_{ab}^{(l)}(\tau)}{2\langle a \rangle \langle b \rangle}. \quad (2.29)$$

There is not shot-noise considerations in equation 2.29. In light scattering experiments, the correction of the shot-noise for Poisson's statistics in the photon count is done by subtracting the mean value of photo counts; $\langle (a^{(0)})^2 \rangle_{i+\tau} \rightarrow \langle (a^{(0)})^2 \rangle_{i+\tau} - \langle a^{(0)} \rangle_{i+\tau}$ [1]. Other type of statistical properties of the photon counts require special attention and those will be treated later on the text.

The systematic error in each join of equation 2.24, introduced by the multi- τ algorithm, is reduced to $\delta s(\tau, \Delta t) = -2\delta g(\tau, \Delta t)$. Another advantage of equation 2.22 is the recycling of the correlation function. For the computation of the structure function, i.e. it is only needed to calculate the terms $\langle (a^{(0)})^2 \rangle_{i+\tau}$ and $\langle (b^{(0)})^2 \rangle_i$.

Chapter 3

Light Scattering

In this chapter we discuss the basic notions of light scattering. We present a discussion of the light scattering techniques and we display the experimental set-ups that we have used in this work. We highlight the dynamic light scattering technique and derive some important results of it. We also review photon statistics, in particular the Mandel's formula and derive some useful results of it.

3.1 Scattering of light

The Scattering theory (ST) is one of the most important and successful frameworks in physics with formulations in terms of classical mechanics, classical electrodynamics and quantum mechanics among others. In simple terms ST studies the dispersion of particles or waves by a potential, for example, in classical mechanics one could ask; how point particles are dispersed by a hard-sphere potential? In more technical terms, ST solves the problem of finding the flux of particles, or radiation, by a potential in a fixed direction known as the differential cross section. Also, one can study the inverse problem of ST , being the differential cross section known, one could determinate the potential which causes the scattering process.

For this work, we are interested in elastic dispersion of laser light, say electromagnetic waves

or photons rather than mass particles and the scatters of interest are colloidal particles, liquid crystal and gels which individual dimensions are less than the wavelength of the light (Rayleigh scattering). The two accessible approaches are: 1) solve the Maxwell equations for the scattered fields and compute the differential cross section, which can be measured experimentally and, 2) the inverse one, which consists in measuring the differential cross section and try to determinate the information about the scatters using previous results. The first of this approaches is complicated due to the equations required to solve and does not led to fruitful results. Due to this, the inverse approach will be used since information about the scatters can be easily determined.

In this context, we understand the scattering process as follows; a known incident light beam with intensity I_o impinges on a sample, it transmits a portion of the incident intensity I_t and scatters another portion I_s . The scattered portion is then collected by a detector in an specific direction, as is shown in figure 3.1, we refer to this set-up as the auto-correlation scheme. In real experiments more complicated set ups are used but this basic idea still holds. Thus, the scattered intensity is the outcome of the scatter process and contains information of the sample. We describe the process in terms of the intensity rather than field because all detectors are sensitive to intensity and not to the field itself.

There are many ways to analyse the scattered intensity, two main techniques must be distinguished; Static Light Scattering (*SLC*) and Dynamic Light Scattering (*DLS*). *SLC* measures the mean scattered intensity as a function of the scattering angle $\langle I_s(\theta) \rangle$. On the other hand, *DLS* measures $I_s(t)$, this is, the scattering intensity as a function of time at a fixed scattering angle. The fluctuations of $I_s(t)$ are a consequence of the nature of the sample.

Since this work, we mostly deal with *DLS*, thus a more detailed description of the experiment is presented in the following sections. Additionally, the so-called photon correlation spectroscopy is introduced together with some important results of correlation and structure functions of the scattered field and intensity.

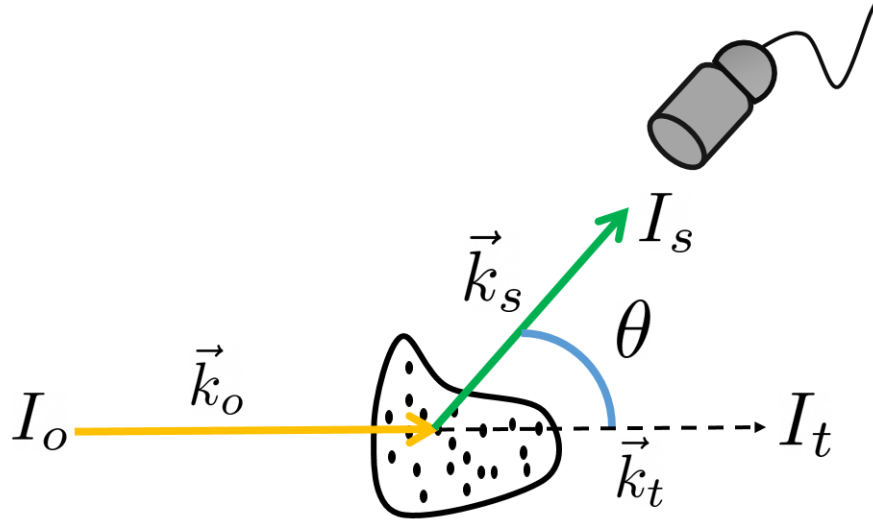


Figure 3.1: Representation of a light scattering experiment. A light beam with intensity I_o and with a wave-vector \vec{k}_o impinges over a volume of the sample. The sample consists of scatterers immersed in a continuous media. The transmitted light is not of interest since it did not interacted with the sample. The scattered light beam is collected at an angle θ , measured with respect to the transmitted beam. The detector used for *SLS* can be a light intensity detector while for *DLS* it must be a photon detector.

3.1.1 Elastic Light Scattering

In the introduction of this chapter we have illustrated the scatter of light by matter, to go on we must take further considerations. The first one is to consider the light source as nearly monochromatic and very stable intensity. This consideration is no unrealistic if one chooses laser light, whose frequency distribution is narrowed. The second is the assumption that each photon, or partial electromagnetic wave, is scattered only one time before being detected; this is possible when the samples are highly dilutes suspensions. The third one is to consider the energy and momentum conservation in each scattering event, the momentum conservation implies $|\vec{k}_o|^2 = |\vec{k}_s|^2$. More general treatments correspond to other beyond the scope of this work.

Let us consider a single photon scattering with a scatterer at position $\vec{x}(t)$. The photon has an initial energy of $\hbar\omega_o$ and momentum of $\hbar\vec{k}_o$. The transfer of energy $\Delta\omega$ and momentum

$\hbar\vec{q}$ of the photon to the scatterer are

$$\hbar\Delta\omega = \hbar(\omega_o - \omega_s), \quad (3.1)$$

and

$$\hbar\vec{q} = \hbar(\vec{k}_o - \vec{k}_s), \quad (3.2)$$

where the subscript o and s refers to incident and scattered light, respectively. In *DLS*, the energy and momentum transfers are typically in the order of $\hbar\Delta\omega \approx 10^0 - 10^{-4}(eV)$ and $q \approx 10^{-4} - 10^{-2}(nm^{-1})$ [15]. This transfer of momentum corresponds to probing internal structures of the sample, which dimensions are in the order of q^{-1} . Studies of $\langle I_s(k) \rangle$ correspond to *SLS* while studies of $\langle I_s(k, t) \rangle$ to *DLS*.

The scattered and incident wave-vector have the same magnitude $|\vec{k}_o|^2 = |\vec{k}_s|^2 = 4\pi n/\lambda_o$, where λ_o is the wavelength of the incident light and n is the effective refractive index of the sample. Due to this, we are able to solve for the magnitude of \vec{q} , a simple calculation leads to

$$|\vec{q}|^2 = |\vec{k}_o - \vec{k}_s|^2 = \frac{4\pi n}{\lambda_o} \sin(\theta/2). \quad (3.3)$$

Thus the scattered photon reaches the detector with energy $\hbar\omega_s$ and momentum $\hbar\vec{q}$. The explicit form of the scattered electric field $E_s(t, \vec{q}_s)$ depends on the position of the scatter and the wave-vector \vec{k} . The scattering process produces a phase change on the photon; therefore, the scattered electric field is $E_s(t, \vec{q}) = E \exp[\phi(t, \vec{k})]$ with $\phi(t, \vec{q}) = \vec{q} \cdot \vec{x}(t)$. The scattered intensity is $I_s(t, \vec{q}) = E_s(t, \vec{q})E_s^*(t, \vec{q})$, where $E_s^*(t, \vec{q})$ is a complex conjugate amplitude of the electric field corresponding to the scattered photon. Without loss of generality, we will write the electric field in a scalar form rather than the vector form.

A natural generalization of the scattering of a single photon is the scattering of a large number of photons. Photons are bosons and they do not scatter with themselves, thereby, the scattered photons are only due to the photon-sample interaction. For the scattering of

a large number of photons we write $E_s(t)$ as

$$E_s(t, \vec{q}) = \sum_{j=1}^N E_j \exp[i\phi_j(t, \vec{q})], \quad (3.4)$$

where E_j and $\phi_j(t, \vec{q})$ are the magnitude and phase function of the $j - th$ planar wave, respectively, and N is the total number of amplitudes scattered in the θ direction.

3.1.2 Cross-correlation experiments

The set-up of figure 3.1 can be generalized to a cross-correlation scheme. This scheme is the combination of two auto-correlation experiments. The advantage of using cross-correlation experiments is that we are not restricted to perform experiments at low molecular mass concentrations, as imposed in auto-correlation experiments [16]. Using cross-correlation we are able to deal with turbid media. In figure 3.2 we show a representation of the set up of a cross-correlation experiment.

Having two different scattered beams impinging over the same volume allows us to eliminate noise in the experiment, e.g, see Ref.[16]. In cross-correlation experiments on turbid media, the resulting multiple scattering contributes only to the background.

3.2 Correlation functions

The scattered field must be treated as a random variable because, even if the incident intensity is constant in time, the scatters in the sample show random movements and; therefore, the photons are randomly scattered in time. In terms of the scattered angle photons are not randomly scattered in general. This is also true in the case of liquid crystals and gels, where the scatters are not moving completely free but they show small random oscillations around their equilibrium positions; and the scattered photons may take random paths through the sample. Therefore, we are able to speak in the context of random functions. We treat

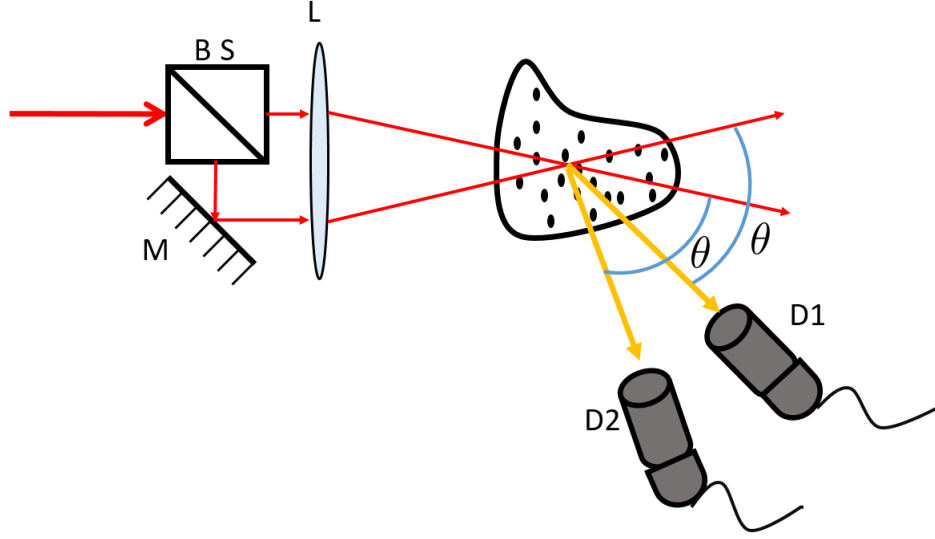


Figure 3.2: Representation of a cross-correlation experiment. A light beam is splitted by a beam splitter (BS). The two beams are directed to the sample by a mirror (M) and a lens (L) and they impinge over the same volume, then the two scattered beams are detected by two different detectors (D1 and D2) at the same scattered angle θ .

$E_s(t, \vec{q})$ as a Gaussian random variable with zero mean.

Information of the sample is hidden in the phase functions, i.e., the fluctuations of the scattered field are a result of the geometrical distribution of the scatters and their movement. To pull out this information, we make use of the correlation functions presented in chapter II.

3.2.1 Correlation function of the scattered field

The first order correlation function of the scattered field is defined as

$$G_E(\vec{q}, t, \tau) = \langle E_s(t, \vec{q}) E_s^*(t + \tau, \vec{q}) \rangle, \quad (3.5)$$

where $\langle \rangle$ stands for temporal average. We will assume a *WSS* process; therefore, the correlation function $G_E(\vec{q}, t, \tau)$ will only depend on the lag-time τ . For simplicity we will

refer to $G_E(\vec{q}, t, \tau)$ as $G_E(\vec{q}, \tau)$. If we insert equation 3.5 into equation 3.4 we obtain

$$G_E(\vec{q}, \tau) = \left\langle \sum_{j=1}^N \sum_{i=1}^N E_i E_j^* \exp[i(\phi_i(0, \vec{q}) - \phi_j(\tau, \vec{q}))] \right\rangle. \quad (3.6)$$

Separating equation 3.6 in two different terms

$$G_E(\vec{q}, \tau) = \left\langle \sum_{j=1}^N |E_j|^2 \exp[i\vec{q} \cdot (\vec{x}_j(0) - \vec{x}_j(\tau))] \right\rangle + \left\langle \sum_{i,j=1, j \neq i}^N E_i E_j \exp[i\vec{q} \cdot (\vec{x}_i(0) - \vec{x}_j(\tau))] \right\rangle. \quad (3.7)$$

After exchanging the sum and the temporal average, $\langle \Sigma \rangle \rightarrow \Sigma \langle \rangle$, the second term of the last equation corresponds to the sum of phase averages of the form $\langle \exp[i\vec{q} \cdot (\vec{x}_i(0) - \vec{x}_j(t))] \rangle$ with the condition $i \neq j$. For the case of colloidal suspensions, where the scatters are in random movement, the phase functions are all independent and uncorrelated; therefore, the mean values of the form $\langle \exp[i\vec{q} \cdot (\vec{x}_i(0) - \vec{x}_j(t))] \rangle$ $i \neq j$ are all equal to zero. This may not be true for crystals and gels, where the scatters are almost fixed in their positions. To evaluate the first term, we assume statistical independence between the amplitude E_i and the phase average. Another assumption is to consider identical scatters in the sample; in consequence, all terms in the sum contribute equally. Thus we get the result

$$G_E(\vec{q}, \tau) = N \langle |E_j|^2 \rangle \langle \exp[i\vec{q} \cdot \Delta \vec{x}_j(\tau)] \rangle, \quad (3.8)$$

where j refers to any scatter in the sample and $\Delta \vec{x}_j(\tau) = \vec{x}_j(0) - \vec{x}_j(\tau)$ represents the displacement of the particle. Now, taking the Fourier transform of equation 3.8 into the space domain, the result is

$$\mathcal{F}[G_E(\vec{q}, \tau)] = \bar{G}_E(\vec{x}, \tau) = \int d^3 \vec{q} \exp(i \vec{q} \cdot \vec{x}) G_E(\vec{q}, \tau) = N \langle |E_j|^2 \rangle \langle \delta(\vec{x} - \Delta \vec{x}_j(\tau)) \rangle, \quad (3.9)$$

where δ is the Dirac delta function. The function $\bar{G}_E(\vec{x}, \tau) d^3 \vec{x}$ is interpreted as the proba-

bility density function of finding a particle in the neighbourhood $d^3\vec{x}$ at time τ and $\bar{G}_E(\vec{x}, \tau)$ obeys a diffusive equation [17]. This differential equation is

$$\frac{\partial}{\partial \tau} \bar{G}_E(\vec{x}, \tau) = D \nabla^2 \bar{G}_E(\vec{x}, \tau), \quad (3.10)$$

where D is the coefficient of diffusion. To obtain an explicit form of equation 3.8, we take the inverse Fourier transform of equation 3.10, this yields

$$\frac{\partial}{\partial \tau} G_E(\vec{q}, \tau) = -q^2 D G_E(\vec{q}, \tau). \quad (3.11)$$

To solve equation 3.11, we set the initial condition $G_E(\vec{q}, 0) = N \langle |E_j|^2 \rangle$. Then, the solution of the equation 3.11 is

$$G_E(\vec{q}, \tau) = N \langle |E_j|^2 \rangle \exp(-q^2 D \tau). \quad (3.12)$$

3.2.2 Correlation function of the scattered intensity

As we mentioned before, the detectors are sensitive to the squared modulus of the electric field and not to the field itself. Therefore, $G_E(\vec{q}, \tau)$ is not directly measurable in the experiment. It is of convenience to define the correlation functions of the scattered intensity $G_I(\vec{q}, \tau)$. We define the correlation function of the scattered intensity as

$$\begin{aligned} G_I(\vec{q}, \tau) &= \langle I_s(0, \vec{q}) I_s(\tau, \vec{q}) \rangle = \\ &= \left\langle \sum_{j,i,q,p=1}^N E_j E_i^* E_q E_p^* \exp(i\vec{q} \cdot (\vec{x}_j(0) - \vec{x}_i(0) + \vec{x}_q(\tau) - \vec{x}_p(\tau))) \right\rangle \end{aligned} \quad (3.13)$$

To evaluate equation 3.13, we use the same arguments as done for $G_E(\vec{q}, \tau)$. Switching the subscripts in equation 3.13 we get the next results.

1. If $j = i = q = p$, then

$$\left\langle \sum_{j,i,q,p=1}^N E_j E_j^* E_j E_j^* \right\rangle = N \langle |E_j|^4 \rangle = \frac{G_E(\vec{q}, 0)^2}{N}. \quad (3.14)$$

2. If $j = i$, $q = p$ and $i \neq p$, then

$$\left\langle \sum_{p=1}^N \sum_{i=1}^{N-1} E_i E_i^* E_p E_p^* \right\rangle = N(N-1) \langle |E_i|^2 \rangle^2 = \left(1 - \frac{1}{N}\right) G_E(\vec{q}, 0)^2 \quad (3.15)$$

3. If $q = i$, $p = j$ and $i \neq j$, then

$$\left\langle \sum_{i=1}^N \langle |E_i|^2 \rangle \exp(i\vec{q} \cdot (\vec{x}_i(\tau) - \vec{x}_i(0))) \right\rangle \left\langle \sum_{j=1}^{N-1} \langle |E_j|^2 \rangle \exp(-i\vec{q} \cdot (\vec{x}_j(\tau) - \vec{x}_j(0))) \right\rangle = \quad (3.16)$$

$$= N(N-1) \langle |E_i|^2 \rangle^2 \langle \exp[i\vec{q} \cdot \Delta\vec{x}_j(\tau)] \rangle \langle \exp[-i\vec{q} \cdot \Delta\vec{x}_j(\tau)] \rangle$$

$$= \left(1 - \frac{1}{N}\right) |G_E(\vec{q}, \tau)|^2$$

Adding equations 3.14, 3.15 and 3.16 and setting $N \gg 1$ we get

$$G_I(\vec{q}, \tau) = G_E(\vec{q}, 0)^2 + |G_E(\vec{q}, \tau)|^2. \quad (3.17)$$

We have obtained an analytic expression for both $G_I(\vec{q}, \tau)$ and $G_E(\vec{q}, \tau)$. In the literature is common to find the normalized form of $G_E(\vec{q}, \tau)$ and $G_I(\vec{q}, \tau)$, these are defined as

$$g_E(\vec{q}, \tau) = \frac{G_E(\vec{q}, \tau)}{N \langle |E_j|^2 \rangle} = \exp(-q^2 D\tau) \quad (3.18)$$

and

$$g_I(\vec{q}, \tau) = \frac{G_I(\vec{q}, \tau)}{(N \langle |E_j|^2 \rangle)^2} = 1 + \exp(-2q^2 D\tau). \quad (3.19)$$

Here we have assumed a perfect detector for the scattered intensity. Detectors have a finite coherence area which produces a reduction in the detected signal [1], this redefines equation 3.19 as

$$g_I(\vec{q}, \tau) = 1 + \beta \exp(-2q^2 D\tau), \quad (3.20)$$

where $0 \leq \beta \leq 1$. For later purposes, we rewrite equation 3.20 in the form of equation 2.19

$$\hat{g}_I^{(2)}(\vec{q}, \tau) = g_I(\vec{q}, \tau) - 1 = \beta \exp(-2q^2 D\tau). \quad (3.21)$$

In the same context, we present a form of the auto-structure function given by equation 2.20

$$\hat{s}_I^{(2)}(\vec{q}, \tau) = \beta(1 - \exp(-2q^2 D\tau)), \quad (3.22)$$

where we have assumed a wide sense stationary process. To deduce equation 3.20 we do not make any distinction if the correlation was cross or auto; therefore, equation 3.20 holds for both operations. On the other hand, the structure function given by equation 3.22 is only valid for auto-structure function. For cross-structure function, we use the following equation

$$\hat{s}_I^{(2)}(\vec{q}, \tau) = \alpha - \beta \exp(-2q^2 D\tau), \quad (3.23)$$

where the constant α is given by

$$\alpha = \frac{G_{aa}(0) + G_{bb}(0)}{2 \langle a \rangle \langle b \rangle}. \quad (3.24)$$

3.3 Photon counts and intensity statistics

Previously we have mentioned that detectors are sensitive to the intensity rather than to the electric field. However, we did not mention any detail of the response of the detector. Photon detectors do not measure $I_s(t, \vec{q})$ (which is a continuous function), instead they measure a discrete form of the scattered intensity n_j , e.g., see figure 3.3. To fully understand the response of the detector, we must consider the scattered beam made up of photons and not by waves. This picture suggest us the quantum nature of the detection process.

When a scattered photon reaches the detector, it hits the detection area of a photon detector and the next events may occur [11]: absorption of a photon by an atom and the energy transfer to an electron of the atom and transport of the electron to the conducting band, electron release from the surface, and finally the current originated by this electron is then amplified and detected, we will refer to this event as a photon event. The detection of a current is the signature of a photon reaching the detector. Moreover, a photo event may not be originated by a photon, an electron can emerge to the surface by thermal agitation introducing noise to the experiment. Also, a photon hitting the sensitive area the detector may not be absorbed, in fact, if a photon is absorbed by an atom and detected or not is determined by the laws of quantum mechanics [18]. Even so, the semi-classical theory gives equivalent results [11].

The raw output of a photon counter is the time between two consequent photo events measured in time units of the detector. The detector has a count frequency f and a time resolution of f^{-1} , thus, the time between two photon events is a multiple of f^{-1} . From the raw data we used a process of segmentation to get a discrete form of the number of scattered photons in the q direction per unit of time n_j with $j = 1, \dots, T$, e.g., see appendix B. n_j is the sum of the scattered photons in a time window of $\Delta t \geq f^{-1}$ (sample time), the subscript j refers to the j th time window and $\Delta t T$ is the total measure time. n_j is a doubly stochastic process since is modelled by two stages, the first is the scattered intensity $I_s(t, \vec{q})$ and the second are the photon events in the detection process. We are interested in the statistical

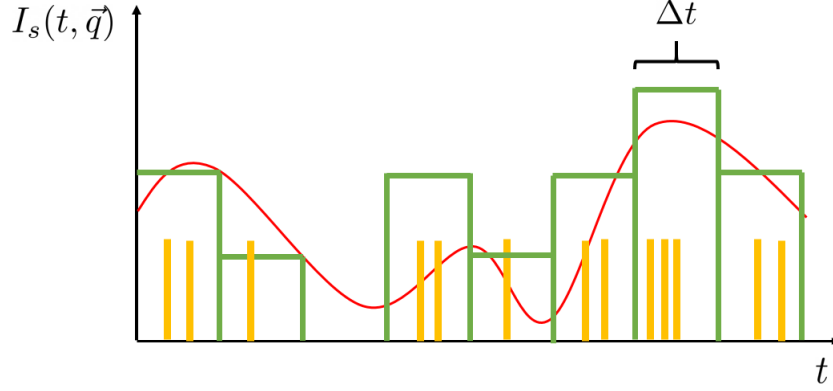


Figure 3.3: Representation of $I_s(t, \vec{q})$ (red line), the photon events (yellow bars) and n_j (green bars). n_j is a discrete function of width Δt . The height of n_j is determined by the number of photon events within its width, for example n_1 is equal to two units, n_2 is equal to one unit and so on.

properties of $I_s(t, \vec{q})$; thus, we must set ways to extract the information of $I_s(t, \vec{q})$ out of n_j .

3.3.1 Photon statistics

Having in hand the discrete form of the scattered intensity, the question of interest is: are the statistical properties of $I_s(t, \vec{q})$ preserved by n_j ? To answer this question, two fundamental properties are proposed [19], here we reformulated them in terms of the detection process. Following the notation of Shatzel [1], we write this conditions mathematically, let $\langle n_j | I_s(t, \vec{q}) \rangle$ indicate the conditional expectation of n_j given $I_s(t, \vec{q})$, then:

- Linearity between the two random process $I_s(t, \vec{q})$ and n_j , $\langle n_j | I_s(t, \vec{q}) \rangle = C I_s(t, \vec{q})$, where C is a constant. This condition is reachable if we stay in the linear response of our detector.
- Second, statistical independence of the counts n_j and $n_{j+\tau}$, $\langle n_j n_{j+\tau} | I_s(t, \vec{q}) I_s(t+\tau, \vec{q}) \rangle = \langle n_j | I_s(t, \vec{q}) \rangle \langle n_{j+\tau} | I_s(t+\tau, \vec{q}) \rangle$. This condition is reachable if the scattered intensity is low and it does not saturate the detector.

The answer to the previous question is, the statistical properties are preserved partially. The

first order statistical properties are not preserved while the second order statistics may be preserved. It is shown by Schatzel that the temporal correlation functions of both processes are equivalent $\hat{G}_n(\tau) = C^2 G_I(\vec{q}, \tau)$ [1]. For the structure function the following relation holds,

$$\hat{S}_n(\tau) = \langle \text{Var} [n_j | I_s(t, \vec{q})] \rangle + \langle \text{Var} [n_{j+\tau} | I_s(t + \tau, \vec{q})] \rangle + C^2 S_I(\vec{q}, \tau). \quad (3.25)$$

These variances are what we call shot-noise after equation 2.29. For a *WSS* process and Poisson statistics, in the photon counts the two variances of equation 3.25 are equal to the mean value of photon counts and contribute only as a baseline. This last case is out of our interest since the case of Poisson's statistics is only found when the scattered intensity is constant over time, as it is shown later in this chapter. A more general and important situation arises when the scattered light is thermal and polarized, in this case the variances of equation 3.25 are equal to

$$\langle \text{Var} [n_{j+\tau} | I_s(t + \tau, \vec{q})] \rangle = \langle n \rangle_{j+\tau} \left(1 + \frac{\langle n \rangle_{j+\tau}}{\mathcal{M}} \right), \quad (3.26)$$

where $\mathcal{M} = \mathcal{M}_t \mathcal{M}_s$ represents the number of degrees of freedom. The term \mathcal{M}_t is the temporal degrees of freedom while \mathcal{M}_s is the spacial degrees of freedom [11]. The Poisson's statistics case is obtained when $\mathcal{M} \gg \langle n \rangle_{j+\tau}$.

3.3.2 Photon counts statistics

From the discrete form of the scattered intensity, an histogram of n_j can be computed. As a result, we have access to the probability density function of n_j , $\mathcal{P}(k)$ with k being the number of photon counts in a sample time of width Δt . The probability $\mathcal{P}(k)$ is estimated in terms of the observed frequency of $n_j = k$. On the other hand, the probability density

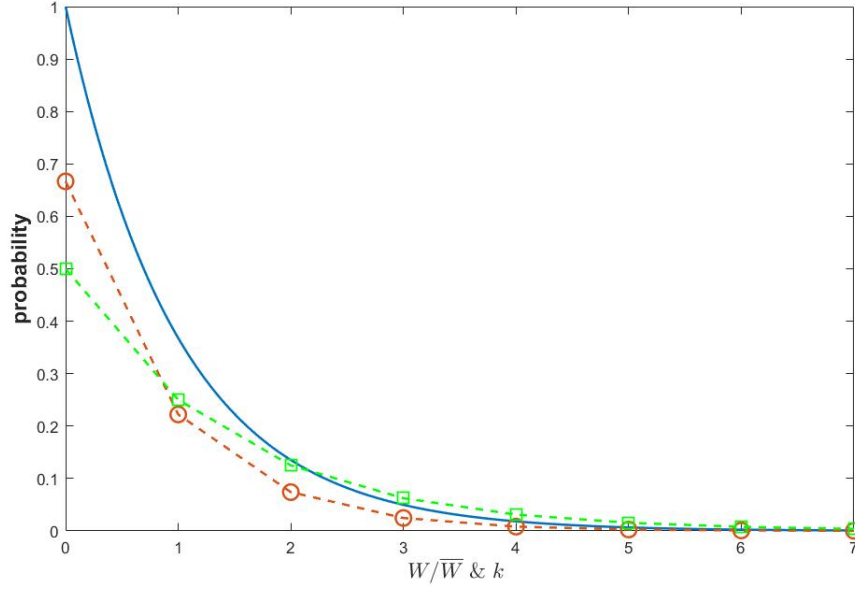


Figure 3.4: Plot of $\bar{W}\mathbb{P}(W/\bar{W})$ for polarized thermal light (blue continuous line). Plots of the distribution of photon counts $\mathcal{P}(k)$ are presented with $\bar{k} = 1$ (green squares) and $\bar{k} = 0.5$ (red circles). The points are joined by a dashed line but only the integer values of k makes sense. It can be seen that the exponential decay of $\bar{W}\mathbb{P}(W/\bar{W})$ is somehow preserved for $\mathcal{P}(k)$.

function of $I_s(t, \vec{q})$, $\mathbb{P}(I_s(t, \vec{q}))$ is related to $\mathcal{P}(n_j)$ by the Mandel's formula [20, 11],

$$\mathcal{P}(k) = \int_0^\infty \frac{(\alpha W)^k}{k!} \exp[-\alpha W] \mathbb{P}(W) dW. \quad (3.27)$$

Here, $\alpha = \eta/h\bar{\nu}$ is a constant where η is the quantum efficiency of the detector, h is the Plank's constant and $\bar{\nu}$ is the mean value of the optical frequency of the radiation. W is the integrated intensity given by

$$W = A \int_{t-\Delta t}^t I_s(z, \vec{q}) dz, \quad (3.28)$$

where A is the photon sensitive area of the detector. If the coherence time of $I_s(t, \vec{q})$, τ_c , is such that $\tau_c \gg \Delta t$ then $W = A\Delta t I_s(t, \vec{q})$. The coherence time of light is understood as the time in which the propagated light is still consider coherent. In the situations we deal the coherent time is excepted to be at least in the order of 10^{-3} s while our sample time is at most in the order of 10^{-5} s.

To show the use of equation 3.27; and for later purposes, we explicitly calculate several forms of $\mathcal{P}(k)$. By considering that the scattered intensity constant in time, this means $I_s(t, \vec{q}) = I_o$; therefore, the integrated intensity is $W = A\Delta t I_o$, which probability distribution is $\mathbb{P}(W) = \delta(W - A\Delta t I_o)$. A simple calculation leads to

$$\mathcal{P}(k) = \frac{(\bar{k})^k}{k!} \exp[-\bar{k}]. \quad (3.29)$$

Here $\bar{k} = \alpha A \delta t I_o = \alpha \bar{W}$ is interpreted as the mean number of photon events. This result highlights the stochastic nature of the detection process, even for the detection of time independent intensity the number of photons detected in a sample time is Poisson distributed. Another example is the polarized thermal radiation, for which the probability density function of the integrated intensity is [11]

$$\mathbb{P}(W) = \frac{1}{\bar{W}} \exp\left[-\frac{W}{\bar{W}}\right], \quad (3.30)$$

where $\bar{W} = A\Delta t \overline{I_s(t, \vec{q})}$ is the mean value of W . A simple calculation leads to

$$\mathcal{P}(k) = \frac{1}{1 + \bar{k}} \left(\frac{\bar{k}}{1 + \bar{k}} \right)^k. \quad (3.31)$$

Equation 3.31 is the geometric distribution. A graphic representation of equations 3.30 and 3.31 is presented in figure 3.4.

Another case of interest is the unpolarized thermal light, whose integrated intensity distribution is [11]

$$\mathbb{P}(W) = \left(\frac{2}{\bar{W}} \right)^2 W \exp\left[-\frac{2W}{\bar{W}}\right]. \quad (3.32)$$

Using Mandel's formula we get the result

$$\mathcal{P}(k) = \left(\frac{2}{2 + \bar{k}} \right)^2 (k + 1) \left(\frac{\bar{k}}{2 + \bar{k}} \right)^k. \quad (3.33)$$

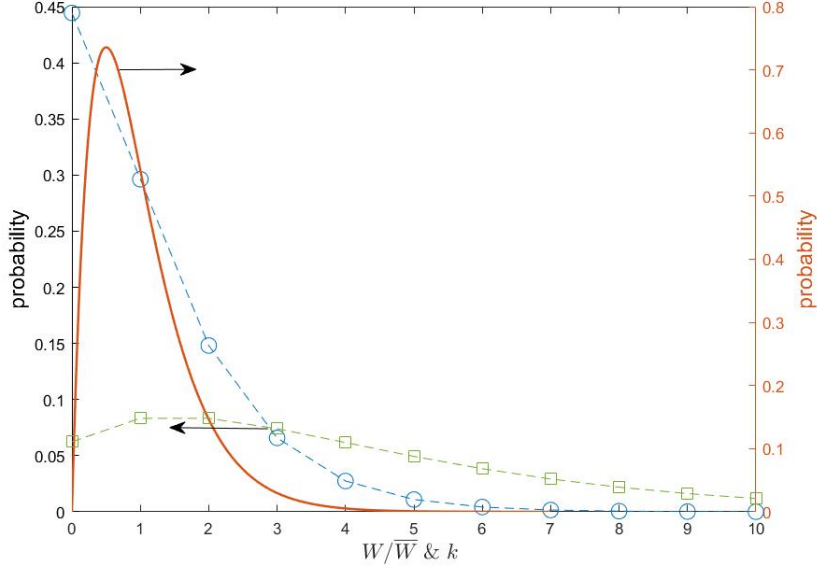


Figure 3.5: Plot of $\overline{W}^2 \mathbb{P}(W/\overline{W})$ for unpolarized thermal light (red continue line plotted in the right axis). Plots of the distribution of photon counts $\mathcal{P}(k)$ are presented with $\overline{k} = 1$ (blue circles) and $\overline{k} = 4$ (green squares). The form of $\overline{W}^2 \mathbb{P}(W/\overline{W})$ is not preserved by $\mathcal{P}(k)$. For $\overline{k} = 1$ $\mathcal{P}(k)$ is a decreasing function, while for $\overline{k} = 4$ it increases and decreases. The two lines meet at $\overline{k} = 2$.

A plot of equations 3.32 and 3.33 is presented in figure 3.5.

Last, we present a more general case: partially polarized thermal light. It's probability distribution is [11]

$$\mathbb{P}(W) = \frac{1}{\mathcal{P}\overline{W}} \left(\exp \left[-\frac{2W}{(1+\mathcal{P})\overline{W}} \right] - \exp \left[-\frac{2W}{(1-\mathcal{P})\overline{W}} \right] \right), \quad (3.34)$$

where $0 \leq \mathcal{P} \leq 1$ is the degree of polarization. Equation 3.30 and 3.32 are particular cases of equation 3.34. It is straightforward to show that when $\mathcal{P} = 1$, the equation 3.35 is reduced to equation 3.31; and, when $\mathcal{P} = 0$ the equation 3.35 is reduced to equation 3.33. The distribution of photon counts is

$$\mathcal{P}(k) = \frac{1}{\mathcal{P}\overline{k} + \frac{2\mathcal{P}}{1+\mathcal{P}}} \left(\frac{\overline{k}}{\overline{k} + \frac{2}{1+\mathcal{P}}} \right)^k - \frac{1}{\mathcal{P}\overline{k} + \frac{2\mathcal{P}}{1-\mathcal{P}}} \left(\frac{\overline{k}}{\overline{k} + \frac{2}{1-\mathcal{P}}} \right)^k \quad (3.35)$$

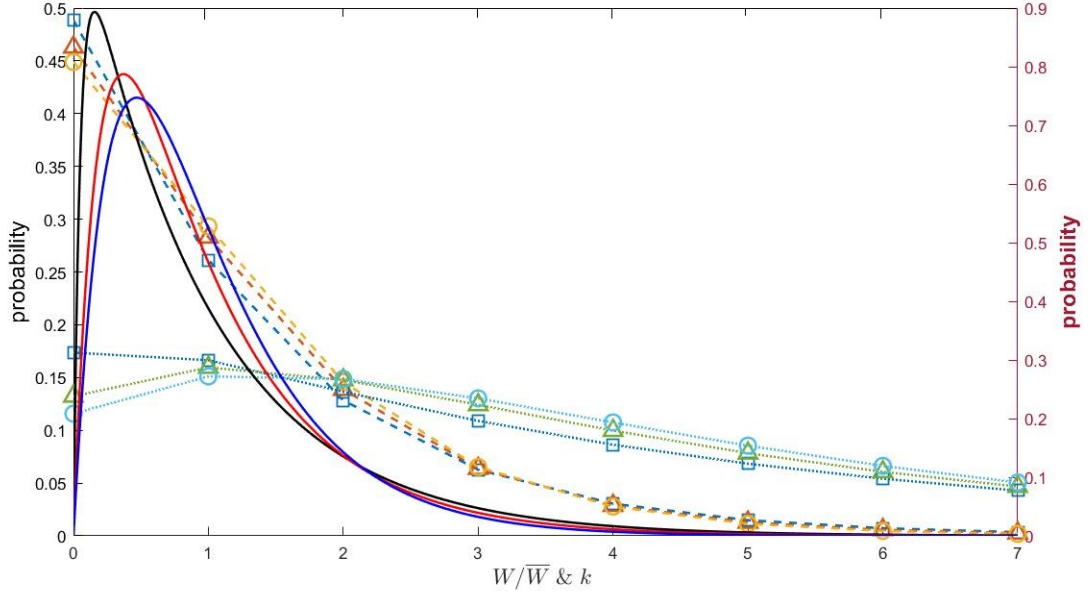


Figure 3.6: Plot of $\overline{W}\mathbb{P}(W/\overline{W})$ using the left y axis for different values of $\mathcal{P} = 0.9$ (black solid line), $\mathcal{P} = 0.6$ (red solid line) and $\mathcal{P} = 0.3$ (blue solid line). The graphs of $\mathcal{P}(k)$ are represented by squares for $\mathcal{P} = 0.9$, triangles for $\mathcal{P} = 0.6$ and circles for $\mathcal{P} = 0.3$. The dashed lines corresponds to $\overline{k} = 1$, while the dotted lines are for $\overline{k} = 4$. The form of $\overline{W}\mathbb{P}(W/\overline{W})$ may not be preserved by $\mathcal{P}(k)$.

We present a plot of equation 3.34 and 3.35 for different values of \overline{k} and \mathcal{P} in figure 3.6. 3.5.

Chapter 4

PhotonSTR – 18

In this chapter, the principal characteristics of *PhotonSTR* – 18 are discussed. We present the time performance, the limitations and the calibration of our software. It is not our intention to display a full explanation of the code, rather we briefly show the architecture of the software and its potential uses. Our software can be free downloaded in the page [21]

4.1 About *PhotonSTR* – 18

4.1.1 Motivation and significance

PhotonSTR – T18 was developed in LabVIEW and can be used to analyze phenomena where there is a fluctuation in the intensity of events over time as it happens in chemical, biological, and other physical processes. *PhotonSTR* – T18 is able to compute sequentially the correlation and structure (*C* & *S*) functions in auto- or cross-mode of time series in off-line mode, the user must have the time series already. Using LabVIEW allows us to parse long sets of data efficiently as processing of data in parallel is native in this programming language, which shortens considerably the processing time. The current version of the program is able to work with binary and *ASCII* files of 8 and 16 bits.

In recent literature, there are works treating the fast calculation of correlation function by

hardware [22, 23, 24] and software [25, 26], to cite some of them. Nevertheless, none of them deals with the structure function, this makes our software interesting for the scientific community. Additionally, the use of hardware to compute the C & S functions might requires the use of graphic cards, fpga cards or other electronic component that may not be accessible by all the users. On the other hand, our software requires only access to LabVIEW and a regular computer, this makes it attractive to the scientific community.

Another appealing feature of *PhotonSTR* – *T18* is its flexibility. A user may modify the software freely according to his necessities. In the current version of the code, it can only analyze zero dimensional point processes but it can be generalized to 2 dimensional processes. We believe that *PhotonSTR* – *T18* can even be implemented in hardware to also work on on-line mode.

4.1.2 Mathematical description

In *PhotonSTR* – *T18* to calculate the C & S functions we use the theory we have developed in chapter 2. More specifically, the C & S are obtained using equations 2.21, 2.23, 2.24 and 2.29. We have mentioned in chapter 3 the equivalence of the correlation function for the random processes $I_s(t, \vec{q})$ and n_i , $\hat{G}_n(\tau) = C^2 G_I(\vec{q}, \tau)$. So we are able to directly interpret the correlation function obtained by the program as the intensity correlation function.

This is not the case for the structure function of the random processes $I_s(t, \vec{q})$ and n_i are not equivalent, as we have already mentioned. The structure function of these two processes are related by equation 3.25. To correctly interpret the structure function of the photon counts as the structure function of the scattered intensity, we must subtract the conditional variances of equation 3.25 or to correct the shot noises mentioned after equation 2.29. The two approaches are totally equivalent.

In the current version of the software, the shot-noises are corrected by the use of equation 3.26, this is

$$\langle (a^{(0)})^2 \rangle_{i+\tau} \rightarrow \langle (a^{(0)})^2 \rangle_{i+\tau} - \langle a^{(0)} \rangle_{i+\tau} \left(1 + \frac{\langle a^{(0)} \rangle_{i+\tau}}{\mathcal{M}} \right). \quad (4.1)$$

To calculate the value of \mathcal{M} it is required an algebraic form of the correlation function of the scattered field, the complex coherence factor and the evaluation of very complicated integrals [11]. We estimate the value of \mathcal{M} using the following algorithm.

- First, we use the points $g_{aa}^{(2)}(\tau = 1)$ and $g_{aa}^{(2)}(\tau = 2)$ to estimate the intercept $\beta \equiv g_{aa}^{(2)}(\tau = 0)$ through an interpolation using a second order polynomial function. We take this intercept as the noise free intercept. This approach is valid when the function $g^{(2)}(\tau)$ can be approximated by a second order polynomial around $\tau = 0$.
- Second, having in hand the noise-free intercept (β) and the noisy intercept ($g^{(2)}(\tau = 0)$) those are related by equation 4.1, which in its normalized form is,

$$\beta = g^{(2)}(0) - \frac{1}{\langle a^{(0)} \rangle_i^2} \left(\langle a^{(0)} \rangle_i + \frac{\langle a^{(0)} \rangle_i^2}{\mathcal{M}} \right). \quad (4.2)$$

From equation 4.2 we solve for \mathcal{M} .

With an estimated \mathcal{M} we can use equation 4.1 to correct the shot-noise and correctly interpret the structure function of the photon counts as the intensity structure function.

4.2 Software calibration

As calibration we analyzed a photon history of 50 s from a *DLS* experiment, where a set-up as described in chapter 5 was used. The sample used was a highly diluted suspension, ($\sim 1 \times 10^{-5}$ in volume fraction), of latex nanoparticles of radius $r = 50nm$ (IKERLAT Polymers, Spain) at a temperature of $20C^\circ$. The calibration consist in estimating the hydrodynamic radius that is reported by the manufacturer $r_H = 50nm$. We use *PhotonSTR-T18* to analyze the raw data and compute the C & S functions using $P = 64$, $m = 2$ and a sample

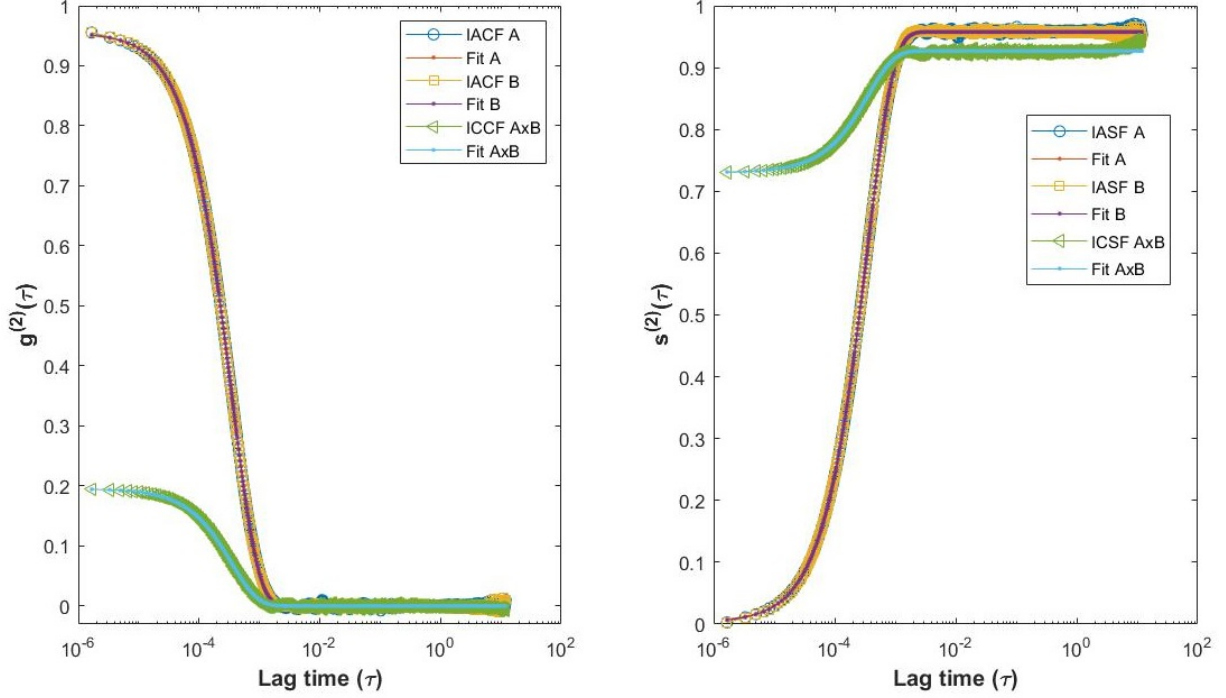


Figure 4.1: Plot of the ICF and ISF functions for the two channels A and B and for the cross-structure function AxB . The continuous lines correspond to the fits.

time of 100. To the C & S functions obtained by our software we fit the following laws,

$$\hat{g}_{ab}^{(2)}(\tau) = \beta \exp(-2q^2 D\tau), \quad (4.3)$$

and

$$\hat{s}_{ab}^{(2)}(\tau) = \alpha - \beta \exp(-2q^2 D\tau), \quad (4.4)$$

where q is the magnitude of the scattering vector, D is the diffusion coefficient of the nanoparticles, which depends on the hydrodynamic radius, and β is a parameter to be determined. The parameter α is equal to β in the case of auto-structure functions and is a free parameter in the case of the cross-structure function. To obtain equations 4.3 and 4.4, we have to assume a wide sense stationary process, use of equations 2.19, 2.20 and 3.21. A plot of the intensity correlations functions (ICF) and the intensity structure functions (ISF) are presented in figure 4.1, where IACF A makes reference to $\hat{g}_{aa}^{(2)}(\tau)$, ICCF AxB to $\hat{g}_{ab}^{(2)}(\tau)$ and

Function	Estimated r_H (nm)
IACF A	52.6
IACF B	52.3
ICCF AxB	51.8
IASF A	52.6
IASF B	52.2
ICSF AxB	53.2

Table 4.1: Estimated radius in the calibration process.

so on.

We estimated the hydrodynamic radius of the nanoparticles using the following relation,

$$D = \frac{kT}{6\pi\eta r_H}, \quad (4.5)$$

where T is the temperature of the experiment, k is the Boltzmann constant, η is the viscosity of the solvent and r_H is the hydrodynamic radius of the nanoparticles. The values we obtain in the calibration process are resumed in table 4.1. In general, we see a good agreement in the estimated hydrodynamic radius with the one reported by the manufacturer ($50nm$).

4.3 Time Performance

Fast data processing is an important aspect in most of the applications using C & S functions. We compared the time performance of *PhotonSTR-T18* programmed in LabView with a version of the same software programmed in MatLab and also with a simple linear Correlator/Structurator programmed in MatLab. We understand the time performance as the total time required to compute the discrete estimators $\hat{g}^{(2)}(\tau)$ and $\hat{s}^{(2)}(\tau)$, including the time used to read and process the raw data. For this performance study we have used a desktop computer with a Intel Core *i5-3570* processor with $32GB$ of ram memory .

To compare the time performance of the three programs we used the auto-mode and time series of length $T = 10^r$ with $r = 5, 6, 7, 8, 9$, the results are presented in figure 4.2 for different values of parameters of the multi- τ algorithm. From these results we justify the

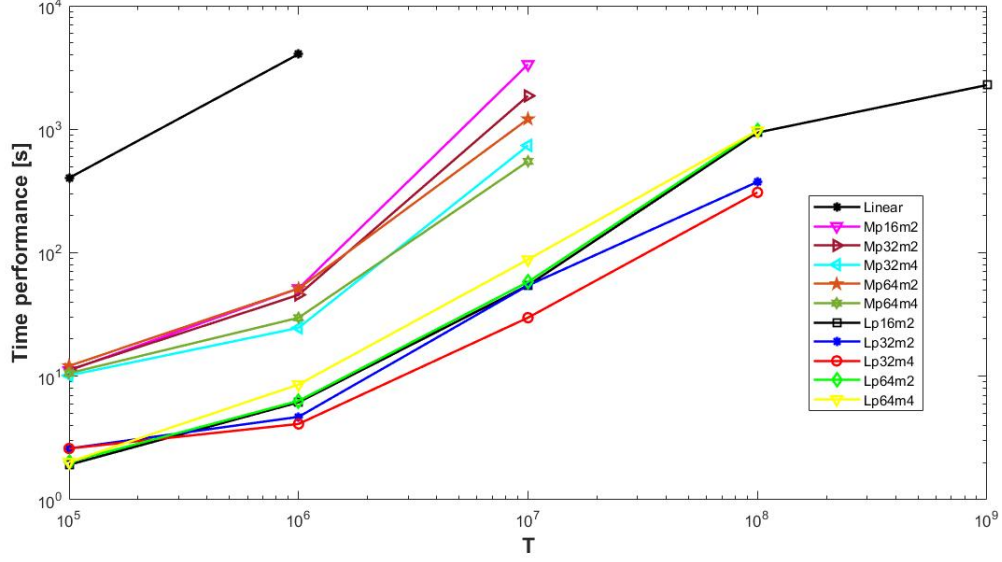


Figure 4.2: Time performance of the three different programs. We used the notation $Mp = x, m = y$ and $Lp = x, m = y$ for Matlab and Labview respectively, with $x = 16, 32, 64$ and $y = 2, 4$. We do not present any result of a run taking more than 3 hours.

choice of LabVIEW as the proper language for our software. Contrary to most of the language programs that execute code sequentially (as Matlab does), Labview runs following a data-flow model[27]. Any code line will be execute when it receives all required inputs, this is a clear advantage for our software since the calculation of all lag times of the C & S functions are independent.

One limitation of our software is presented in figure 4.2, the memory runs out when we analyse time series of length ($> 10^8$). Only the configuration $P = 16, m = 2$ was able to compute the operations when $T = 10^9$. The other configurations of the multi- τ algorithm made the computer run out of ram memory. In our experience it is not common to deal with time series of length $T > 10^9$ in practice, most of the time series are in the order of $10^6 - 10^7$.

Any attempt to run the MatLab programs in parallel will of course reduce the time processing of data. The reduction of this time will depend on the number of cores of the computer one uses, a priori the time processing will be reduced in C^{-1} , where C is the numbers of cores of the computer. As a reference, nowadays the maximum number of cores in a desktop

computer is 10. Even if the MatLab code would run in parallel, it will not overcome the LabVIEW performance. This last discussion applies to any non data flow programming language.

Chapter 5

Experiments

In this chapter we give a brief description of the apparatus we have used to perform our light scattering experiments. We show the synthesis of our samples as well. We present results of the correlation and structure functions C & S that we have obtained using our software *PhotonSTR* – 18 together with an analysis of the functions.

5.1 Experimental setup

The spectrometer used is a 3D LS spectrometer (LS Instruments AG, Switzerland). The spectrometer works with a He-Ne laser that emits light at a wavelength of $\lambda = 632.8\text{ nm}$ and possesses two avalanche photodiodes (APD) as detectors (EXCELITAS SPCM-AQRH-13-FC). We will refer to the data measured by each APD as detector channel A and channel B. The APD's have a photon detection efficiency of $\approx 62\%$ at $\lambda = 650\text{ nm}$, a dark count of 250 counts/sec and a dead time of 50 ns . The spectrometer has a motorized goniometer with a resolution of 0.1° to perform scattering experiments in the range 30-130 degrees. The samples are in a thermal bath to control the temperature of the samples.

In figure 5.1 a set-up of the 3D LS spectrometer is presented. In the appendix A we present a calibration of our apparatus. More details on this device and its features are given, for example, in references [13] and [16].

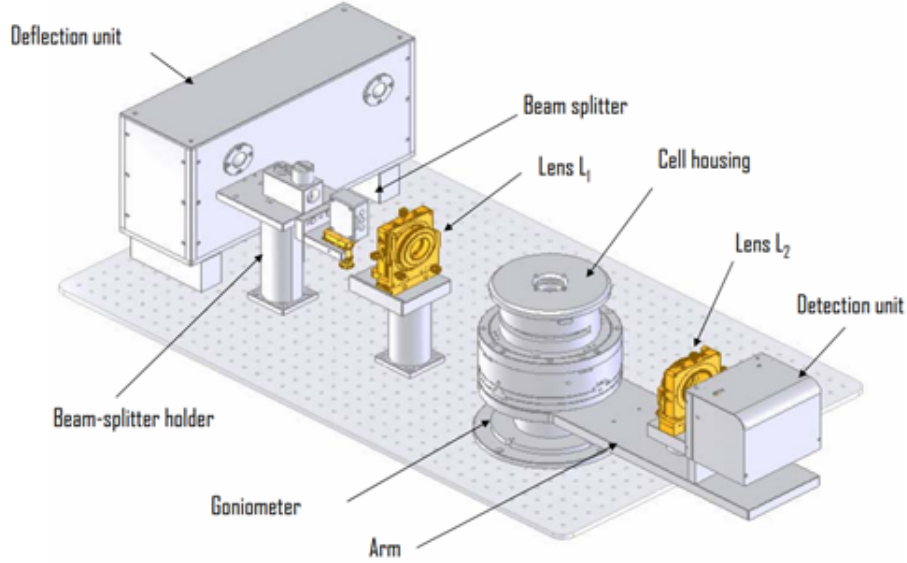


Figure 5.1: 3D LS Spectrometer set-up. The laser light first enter to the Deflection unit to be directed to a beam splitter. Then, the light is split in two beams and directed to the sample by the lens L_1 . The sample is kept in the Cell housing unit, where it is maintained at a fixed temperature by the thermal bath. The scattered photons are directed to the lens L_2 and then to the Detection unit, where they are collected and recorded by the detectors channels A and B. The Detection unit is assembled with the Goniometer by an arm. The optical alignment is such that any effect due to light refraction of light is compensated in the thermal bath.

The manufacturer of the 3D includes with it a digital correlator Flex03lq (correlator.com). This device allows the user to compute the correlation function of the scattered photons in real time or to measure directly the photon history. We avoid the use of the correlator by directly measuring the photon history from the experiments for later analysis. From this data we compute the sample functions of the processes by a segmentation process (see the appendix B), and later use the software *PhotonSTR* – 18 to compute the C & S functions.

5.2 Samples

We chose two different samples for our study, both have in common that are samples that not produce a wide sense stationary process in a light scattering experiment. In this section, we briefly describe the synthesis and some properties of this samples, a more detailed description

is given in references [13, 16, 28].

5.2.1 Polymer matrices of polyacrylamide

The polymer matrices have a total weight concentration of monomer of 2.5% with different quantities of crosslinker bisacrylamide. The cross-linking content can be estimated as,

$$f_{bis} = \frac{m_{bis}}{m_{bis} + m_A} \times 100\%. \quad (5.1)$$

The mass of bisacrylamide used in the synthesis is m_{bis} , and of acrylamide monomer is m_A . Before the polymerization process, latex spheres of $\approx 110nm$ diameter were added to the samples at 0.02% in volume fraction. The concentration of particles is high enough to particles scatter much more light than the polymer matrix but not very high to avoid multiple scattering. In all cases, the systems are kept in sealed cylindrical glass cells.

5.2.2 PNiPAM microgels

We use PNiPAM microgels synthesized by using the standard dispersion polymerization described by Senff and Richtering [29]. We produce quasideionized samples by putting the microgel dispersion in contact with ionic exchangers (Amberlite IRN-150) in sealed quartz cells. The number concentration of the final stock dispersion is estimated from the Bragg peak positions that appears in the crystalline samples [30].

5.3 Results

From the photon history obtained by the light scattering experiments we used our software to do an off-line analysis. All correlation and structure functions were obtained by our software using the configuration $P = 64$, $m = 2$ and a sample time of 1000.

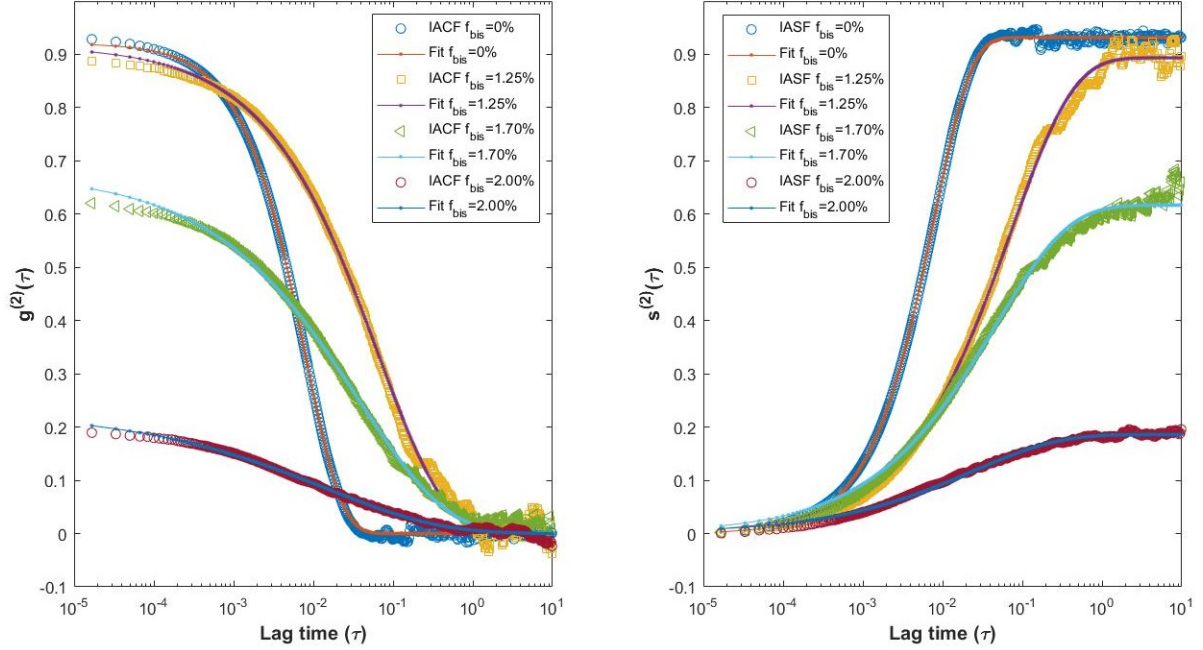


Figure 5.2: (*IACF* & *IASF*) functions for the four different samples. Continuous lines are the fitting results.

5.3.1 Polymer matrices of polyacrylamide

We use four different samples varying the cross-linking content as; $f_{bis} = 0, 1.25, 1.70$ and 2.00% . We perform the scattering experiments at an angle of 90° , use a time measurement of $100s$ for all the samples and a temperature of $20C^\circ$. In figure 5.2, the intensity auto-correlation and structure functions (*IACF* & *IASF*) are presented. To make a qualitative analysis of the results, we fit a generalization of equations 4.3 and 4.4 to the data. These models are,

$$\hat{g}^{(2)}(\vec{q}, \tau) = \beta \exp(-2[\tau/\tau_o]^\gamma), \quad (5.2)$$

and

$$\hat{s}^{(2)}(\vec{q}, \tau) = \beta(1 - \exp(-2[\tau/\tau_o]^\gamma)), \quad (5.3)$$

where γ is the stretching exponent and $\tau_o = q^2 D$ is the decay time. When $\gamma = 1$ we get equations 4.3 and 4.4. In the fitting process we use γ , τ_o and β as free parameters. The resulting parameters from the fitting are presented in table 5.1. The highest value of γ

	$f_{bis} = 0\%$	$f_{bis} = 1.25\%$	$f_{bis} = 1.70\%$	$f_{bis} = 2.00\%$
τ_o (ICCF)	0.0164	0.2475	0.2162	0.1431
τ_o (ICSF)	0.0165	0.2520	0.1992	0.1327
γ (ICCF)	0.9403	0.5199	0.3984	0.3033
γ (ICSF)	0.9185	0.5500	0.4730	0.4098

Table 5.1: Values of γ and τ_o obtained in the fitting process using the model *IACF* & *IASF*.

corresponds to the sample in which the tracers' motion is closer to pure diffusive motion in a continuous medium [13]. On the other hand, as the concentration of f_{Bis} increases, both the decay time and the stretching exponent γ decrease, indicating sub-diffusive motion of the tracers as the network becomes rigid. Our analysis is consistent with previous results [13] and indicates that equations 5.2 and 5.3 are reliable functions to characterize soft condensed materials.

5.3.2 PNiPAM microgel colloids

We used a single sample having a concentration of $n = 102 \text{ part}/\mu\text{m}^3$, calculated considering a microgel's radius $R_M = 120 \text{ nm}$ at $T = 20^\circ\text{C}$. In figure 5.3, we present the static scattered intensity of the sample, as described in previous works [16, 31], this device enables us to determine the single scattering contributions of moderately turbid samples in dynamic and static light-scattering experiments. To obtain ensemble-averaged estimates of the scattered intensity $I_S(\theta)$ for the nonergodic systems, such as those forming crystals, we slowly rotate the samples during data acquisition. Two peaks are observed in $\theta \approx 61^\circ$ and $\theta \approx 120^\circ$, we will refer to the peak at $\theta \approx 61^\circ$ as the principal peak. In figure 5.3, we plot the principal peak with a better angular resolution. The relative position of the peaks highlights the crystalline structure, the bragg's planes identified (labels in the figure) indicate a BCC-like crystalline lattice.

We perform dynamic light scattering experiments at the position of the half width half maximum of the principal peak, $\theta \approx 60.7^\circ$. In figure 5.4 and 5.5, we plot the ICCF's and the ICSF's of four different measurements of 10s duration. In figures 5.4 and 5.5, the same

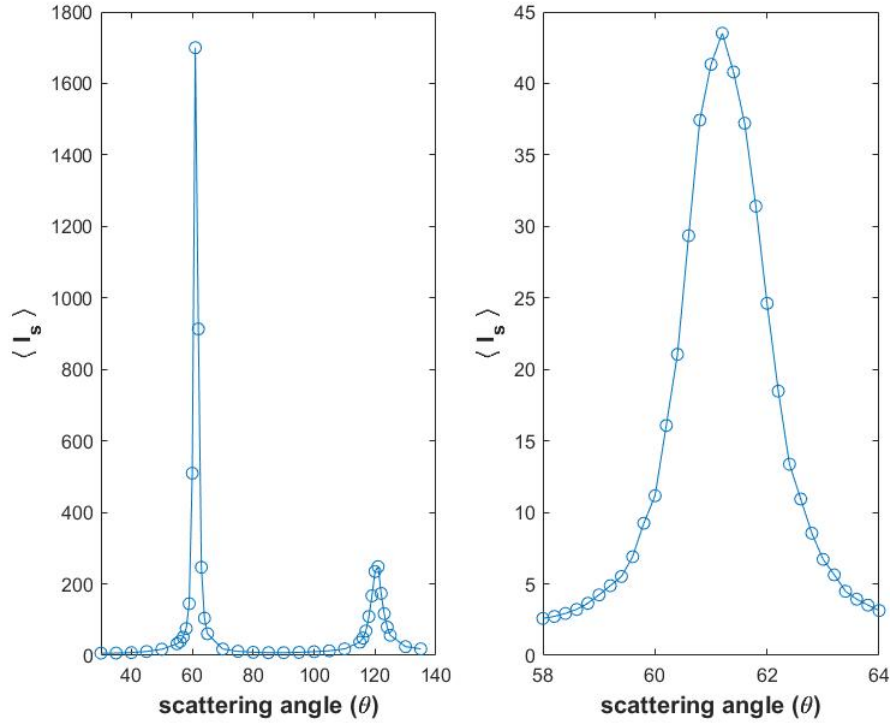


Figure 5.3: Principal peak of the static scattered intensity of the sample *C5* (left) and the principal peak with a higher angular resolution (right).

measurements share the same color and markers, for later purposes we label this measurements as: measurement 1 for red squares, measurement 2 for yellow circles, measurement 3 for purple triangles and measurement 4 for blue diamonds. Despite the labels the measurements were not consecutive obtained in the experiments, these were selected since are the most representative of the complete set of measurements. All functions were obtained by our software using the configuration $P = 64$, $m = 2$ and a sample time of 1000.

We observed some unexpected results in both correlation and structure functions. The correlation function of figure 5.4 passes from being a decreasing function (red squares and yellow circles) to be almost flat (purple triangles) to later be an increasing function (blue diamonds). The same occurs with the structure function in figure 5.5, it passes from being an increasing function (red squares and yellow circles) to be a flat curve (purple triangles) to be a decreasing function (blue diamonds).

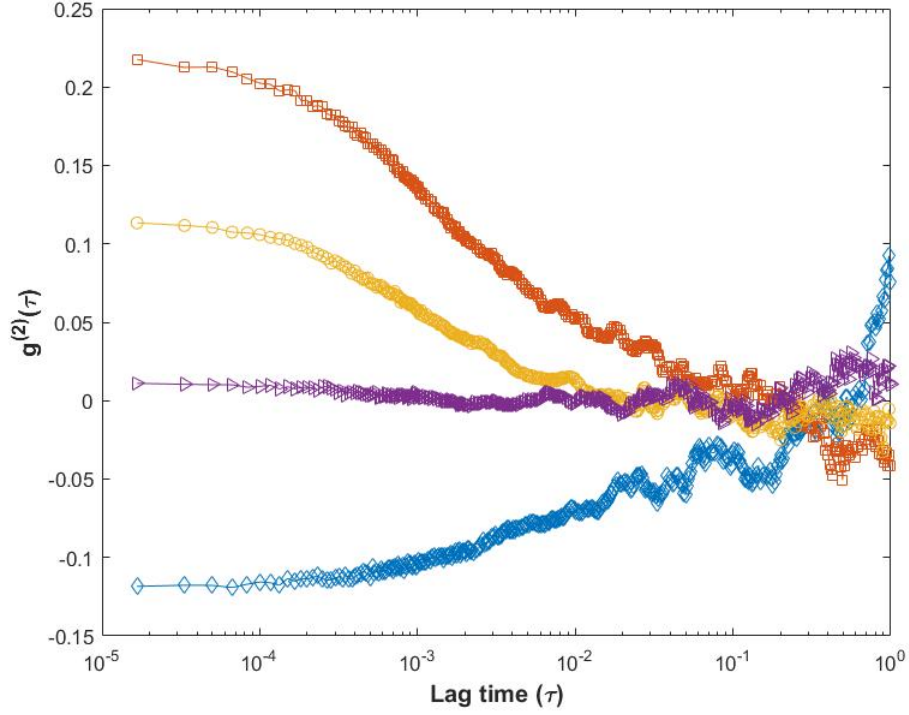


Figure 5.4: Intensity cross-correlation functions of four different measurements.

In the literature, a common practice is to classify the nature of light by the value of the auto-correlation function $g^{(2)}(\tau \rightarrow 0)$ [32, 33]. If $g^{(2)}(\tau \rightarrow 0) > 0$, then the light is recognized to represent a thermal state. If $g^{(2)}(\tau \rightarrow 0) = 0$, then the light is identified to represent a coherent state. Finally, if $g^{(2)}(\tau \rightarrow 0) < 0$, then the light is considered to correspond to a pure quantum state (number state). Additionally, the increasing or decreasing behavior of the correlation function is interpreted in the following way: (i) if the correlation function is a decreasing function, then this is an evidence of the bunching of photons, as is suggested by the classical experiment of Brown and Twiss [34]. (2) When the correlation function is a increasing function, then the anti-bunching of photons may be present [35, 36]. Despite these facts, we make a further analysis of our data.

One of the advantages of having access to the photon history, working in off-line mode, is that we are able to do different analysis rather than only the correlation function. In figure 5.6, we plot the time series of the photon counts by using a sample time of 5×10^6 . Although

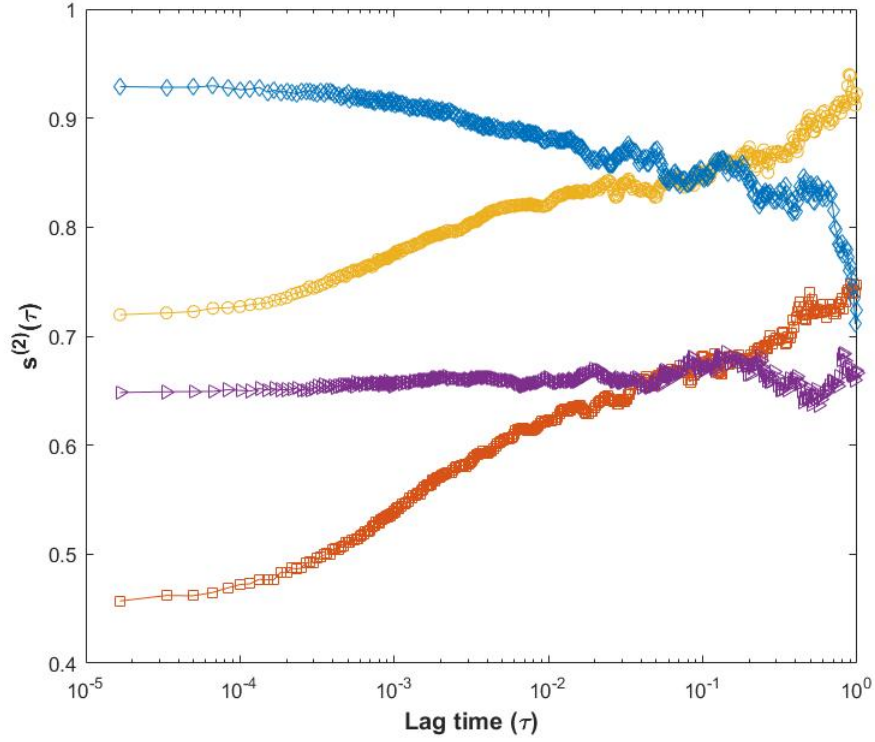


Figure 5.5: Intensity cross-structure functions of four different measurements.

the structure and correlation function above were obtained with a much more smaller sample time, these plots will give us an idea of what is happening.

In figure 5.6, we can observe other behaviour in the time series. In the first graph of the same figure, the red curve is almost always above of the blue one, in other words, the mean value of the photon counts of the detector channel B is greater than the one from channel A. The same occurs in the first six seconds of the measurement 2, and later the two curves fluctuate around a well defined mean value. In measurement 3 there are time windows where the blue curve is above the red one and time windows where both curves fluctuate with approximately the same mean value. Lastly, in the measurement 4 we can observe how the blue curve is above the red one, then the red one is above and so on for the first 8 seconds: the maximum mean value of the photon count is alternating between the two detectors channels. This last behaviour is observed along the four measurements. This suggest us that the sample is acting as a "light scattering modulator", the light scattered by can be negative correlated

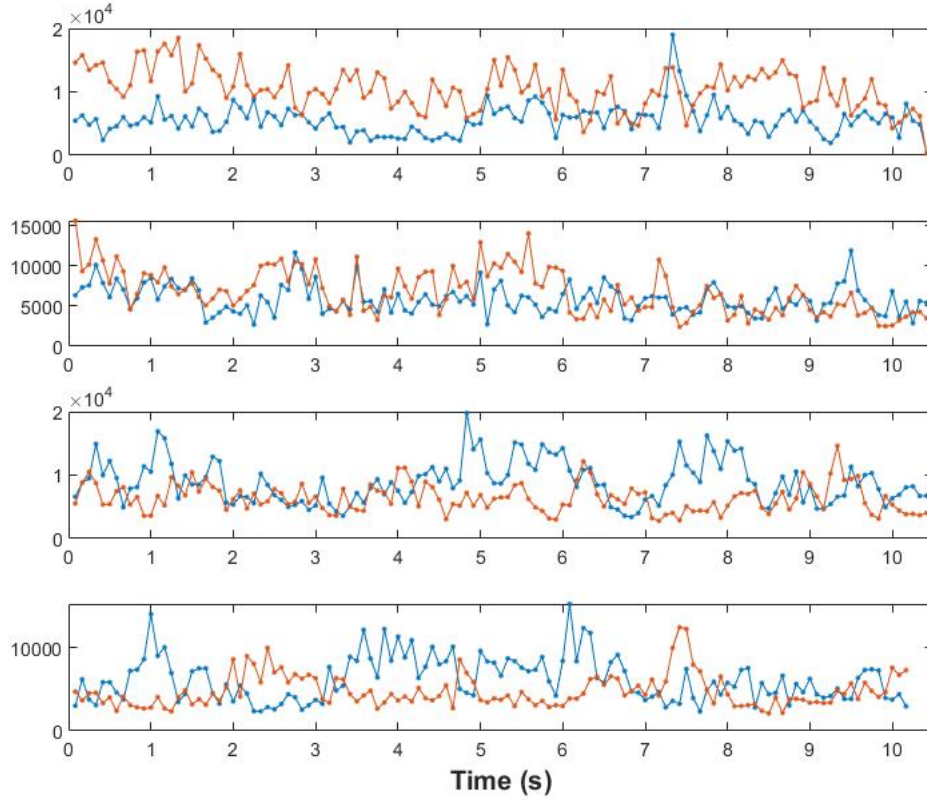


Figure 5.6: Photon counts of the different measurements. The first plot corresponds to the measurement 1, the second to the 2 and so on. In the four graphs, the blue curve refers to the detector channel A and the red one to channel B. We can observe how the mean value of the time series is changing, which is a signature of a non-stationary process.

(measurement 4) and also positive correlated (measurement 1 and 2) and it can also be in intermediate steps (measurement 3).

To go even further, we compute the probability density function of the photon counts n_j , $\mathcal{P}(k)$ by using the histogram of the time series and fitting the expression given in equation 3.35. We use this function since we supposed that the scattered intensity from the sample has an arbitrary degree of polarization. In this step, we used a sample time of 1000 and assumed that this time is much less than any coherence time of the sample. As a first approximation to the problem we use the value \bar{k} of the data and only let as fitting parameter \mathcal{P} in the fitting process. The results are presented in figure 5.7. The results from the fitting process are presented in table 5.2, additionally, the mean value of the photon counts is also

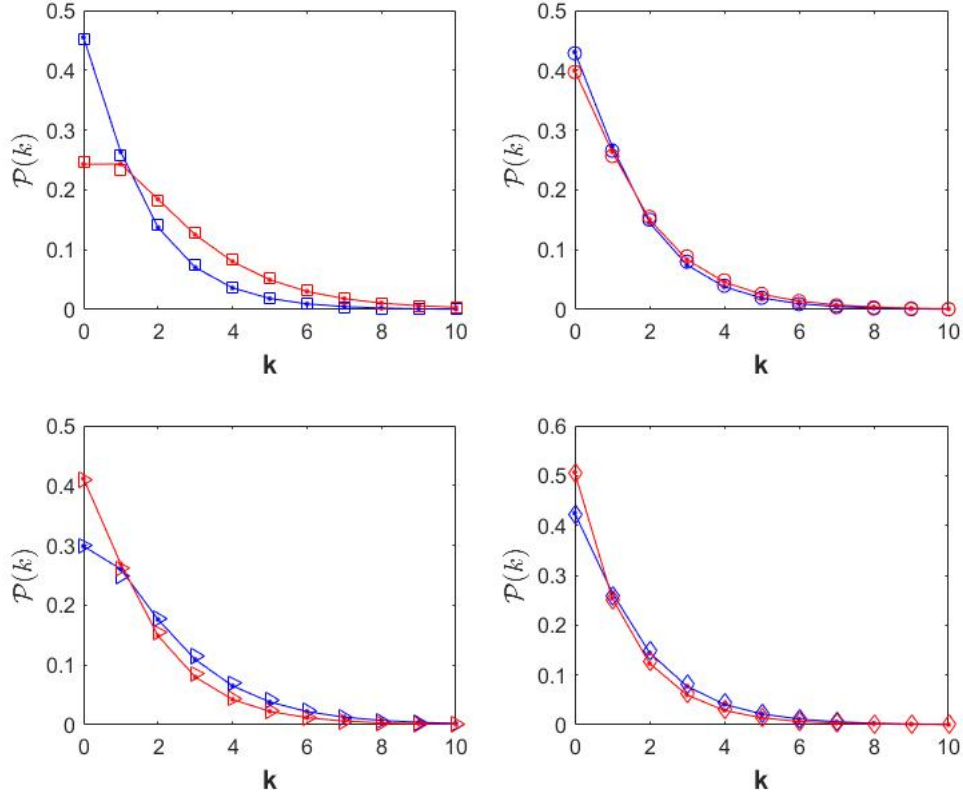


Figure 5.7: Probability density function $\mathcal{P}(k)$ of the four measurements. Only values from $k = 0$ to $k = 10$ are shown, higher values have almost zero probability. In general, we see a good agreement between the data and the fits.

reported. As reference, the value of \mathcal{P} estimated by the same fitting process of suspension of latex nanoparticles used in the calibration of the 3D spectrometer (see appendix A) was for both detector channels $\mathcal{P} \approx 0.99$.

From table 5.2, we can see how the polarization of the scattered light is time dependent as well as the mean number of photon counts. Purcell suggest that the output of a split beam of non-polarized electron that fall into two different electron multipliers would be negative correlated [37]. Here we observe other phenomena, the polarization of the negative correlated scattered light (M4) is closed to unity in both channels, while the polarization of the ‘most positive’ correlation (M1) is closed to 0.3 for one channel and 0.9 for the other one. The values of the polarization changes again for M2 and M3. This suggest us that the negative

cross-correlation may be caused partially for the photon count rate and the polarization of the light.

	M1	M2	M3	M4
\mathcal{P} A	0.8738	0.7559	0.5271	0.8343
\mathcal{P} B	0.3120	0.8179	0.7804	0.9659
\bar{k} A	1.1239	1.1703	1.7784	1.2386
\bar{k} B	2.1107	1.3529	1.2709	0.9593

Table 5.2: Values of the parameters \mathcal{P} and \bar{k} of the four measurements for both detector channels A and B. M1 stands for measurement 1 and so on.

Chapter 6

Discussion and Concluding Remarks

In this work, the software *PhotonSTR* – 18 is presented, it is capable of computing the correlation and structure functions of time series in the off-line mode. We showed a calibration of the software together with a time performance of it. In the calibration, we use both intensity correlation and structure functions from a light scattering experiment to estimate the hydrodynamic radius of a highly diluted suspension of latex nanoparticles. The analysis of both functions gave satisfactory results. The time performance showed the advantage of using LabView, since it takes a shorter time to compute time series using LabView as compared, for example, with MatLab.

We also presented the theoretical background for our software. We have extended a multi- τ algorithm for the intensity correlation function to the structure function, which allows a fast calculation of the structure function. We also put forward a semi-empirical algorithm to remove the conditional variances (or shot-noise) that naturally appear in the photon counts structure function. This allows us to correctly interpret the photon counts structure function as the intensity structure function, in the context of light scattering experiments.

To show the use of *PhotonSTR* – 18, we analyzed data from dynamical light scattering experiments of polyacrylamide networks. Our results were consistent with previous results. We consider that the structure function may be better to characterize non-stationary time

series as indeed produce this kind of systems.

The other system we analyzed is PNiPAM microgel colloidal systems, which showed some unexpected results. The cross-correlation functions, as well as the cross-structure functions, exhibited a peculiar behaviour. For example, the intensity cross-correlation functions passed from being a decreasing to a increasing function as time evolves. From the analysis of the photon history and taking into account polarization effects in the detected signal, we were able to put forward an hypothesis of what causes the observed phenomena. We believe that the PNiPAM microgel colloidal systems are acting as a "light scattering modulator" since the light scattered by it can be positive-correlated and negative-correlated randomly (in a first approximation) as time evolves. Also, we believe that the light polarization of the scattered light contributes to the phenomena since we associate with the multiple scattering of light. Nevertheless, we are far from a complete description of the observed phenomena.

As future work, we propose to translate *PhotonSTR* – 18 to hardware to be able to work in on-line mode. Also, we expect to find the advantages of the use of the structure function upon the correlation function to non-stationary phenomena. And last, extend our experiments and theoretical models to fully understand what causes the negative cross-correlation that we have observed in the PNiPAM microgel colloidal systems.

Appendix A

Calibration of the 3D LS Spectrometer

For the calibration of the 3D LS Spectrometer we used an standard method. We perform a cross-correlation light scattering experiment using a highly diluted suspension, $\sim 1 \times 10^{-5}$ in volume fraction, of latex nanoparticles of radius $r = 50nm$ (IKERLAT Polymers, Spain). If one has a perfect alignment, a clean model sample and laser light with a perfect Gaussian profile, the following condition should be met $g^{(2)}(\tau \rightarrow 0) = \beta \rightarrow 0.25$ in a cross correlation experiment. By a clean and model sample we mean that the latex particles are all perfect spheres with a unique radius and the absence of any dirtiness in the sample.

In figure A.1, we plot the intercept ($g^{(2)}(\tau \rightarrow 0)$) as a function of the scattered angle θ for $\theta = 30 - 135^\circ$. Each point represents the average of measuring the static scattering intensity for 60s. The values for the intercept are below 0.20, we attribute this to any imperfection in the spectrometer, the non-perfect Gaussian profile and dirtiness in the sample. Nevertheless, based on the 3D LS manufacturer specs, We consider this is a good calibration.

In figure A.1 (right y axis), we plot the mean scattered intensity $\langle I_{ss}(q) \rangle$ as a function of the scattered vector q for $\theta = 30 - 135^\circ$ as obtained from averaging the signal over 60s. We fit the static scattering intensity, form factor, using a model for perfect spheres [17],

$$P(q) = P_0 \left[\frac{3}{(qr)^3} (\sin(qr) - qr \cos(qr)) \right]^2. \quad (\text{A.1})$$

Here P_0 and r are the parameters to be determined. The estimated radius obtained from the fitting process is $r = 52 \text{ nm}$.

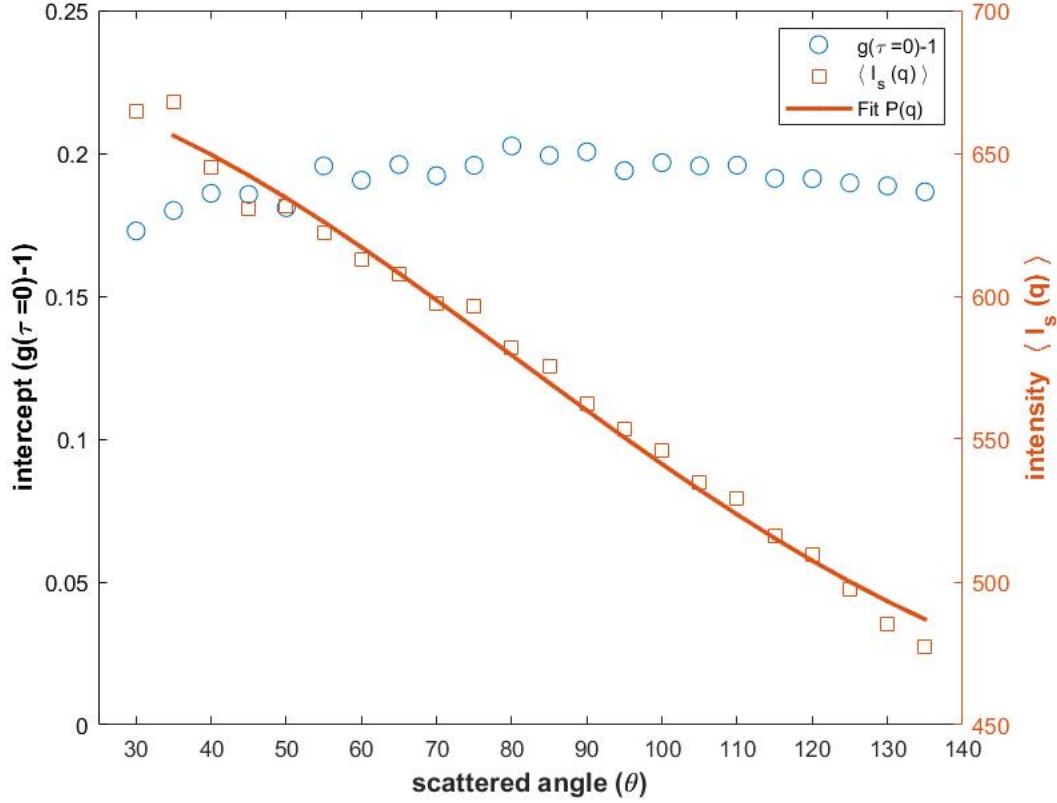


Figure A.1: Intercept $g^{(2)}(\tau \rightarrow 0)$ (left y axis) and $\langle I_s \rangle$ (right y axis). The continuous line corresponds to the fit with the model described in the text.

Appendix B

Data segmentation process

In a light scattering experiment photons are scattered by a sample and recorded in a fixed direction by an instrument which measures the time of arrival of individuals photons, we refer to this as the photon history. In our setup, this is done using a photon-detector (PD) to detect the scattered photons and a photon-counting (PhC) to count the time of arrival of them. Each time a photon is detected by the PD it sends a voltage signal to the PC which records the time at which the signal was received using an internal clock. It is important to note that, due to the quantum nature of the detection process, a photon can enter the PD and not be recorded. Our PhC (flex03lq-12 from correlator.com) has a frequency of $f = 60MHz$ while our PD has a dead time of $50ns$.

The PhC outcome in a light scattering experiment is a file of N 8 *bit* numbers that are later transformed to decimal numbers. The internal clock of the PC runs in cycles of 0 to 255 in time units of f^{-1} . If a photon is detected in a cycle, then the PC records the time when the photon was detected in a number from 0 to 254. If no photon is recorded in the cycle, it starts again and the number 255 is recorded. The recovery time between each cycle is one unit time; thus, N represents the total number of cycles and each 8 *bit* number the time of arrival of the photon in the $n - th$ cycle. Using the output file from the PhC , the total 8 *bit* numbers of photons recorded, its arrival time and the total time of measurement can

be computed.

The final outcome of a *PC* is then a file which contains the time separation of two distinct photon events. For example, the following data 123, 255, 75, 201, ... is interpreted as follows: a first photon was detected at time 123, the second was detected at time 331 and the third at time 532. The number 255 is taken as no photon detected. Following this procedure, we compute the times at which the photons where detected, 123, 331, 532,

The segmentation process then consist in averaging the total number of photons recorded in time windows of fixed width $\Delta t = kf^{-1}$, where k is an integer and we will refer to it as the sample time. As an example, if $k = 1000$ the segmentation process consist in counting how many photons were detected in the time windows 0 – 999, 1000 – 1999 and so on. The result of this corresponds to the scattered number of photons in the j th time window of kf^{-1} , n_j . Mathematically we represent this as

$$n_j = \frac{k}{f} \sum_{j-th \text{ time window}} \text{photons detected.} \quad (\text{B.1})$$

The segmentation process can be understood in the context of any time-dependent measurement. If a detector has a frequency of f , the discrete time-dependent measurement a_j is

$$n_j = \frac{k}{f} \sum_{j-th \text{ time window}} \text{data recorded.} \quad (\text{B.2})$$

Bibliography

- [1] K. Schätzel, “Correlation techniques in dynamic light scattering,” Applied Physics B, vol. 42, pp. 193–213, Apr 1987.
- [2] G. H. Fredrickson and H. C. Andersen, “Kinetic ising model of the glass transition,” Phys. Rev. Lett., vol. 53, pp. 1244–1247, Sep 1984.
- [3] C. Donati, S. C. Glotzer, and P. H. Poole, “Growing spatial correlations of particle displacements in a simulated liquid on cooling toward the glass transition,” Phys. Rev. Lett., vol. 82, pp. 5064–5067, Jun 1999.
- [4] E. O. Schulz-DuBois, Photon Correlation Techniques in Fluid Mechanics. 1981.
- [5] K. Schätzel, “Noise in photon correlation and photon structure functions,” Optica Acta: International Journal of Optics, vol. 30, no. 2, pp. 155–166, 1983.
- [6] K. Schätzel, “Noise on photon correlation data. i. autocorrelation functions,” Quantum Optics: Journal of the European Optical Society Part B, vol. 2, pp. 287–305, aug 1990.
- [7] D. Magatti and F. Ferri, “Fast multi-tau real-time software correlator for dynamic light scattering,” Appl. Opt., vol. 40, pp. 4011–4021, Aug 1999.
- [8] M. S. Z. Kojro, A. Riede and W. Grill, “Systematic and statistical errors in correlation estimators obtained from various digital correlators,” Review of Scientific Instruments, vol. 70, no. 12, pp. 4487–4496, 1999.

- [9] E. O. Schulz-DuBois and I. Rehberg, “Structure function in lieu of correlation function,” Applied physics, vol. 24, pp. 323–329, Apr 1981.
- [10] C. Oliver and E. Pike, “Statistical accuracy in the photon counting structure function of fluctuating light fields,” Optica Acta: International Journal of Optics, vol. 28, no. 10, pp. 1345–1358, 1981.
- [11] J. W. Goodman, Statistical Optics. 2015.
- [12] C. A. García-Cadena, A. de J. Aguilar-Urbe, and L. F. Rojas-Ochoa, “Photonstr-18: A labview toolbox for photon correlation spectroscopy,” SoftwareX, vol. 13, p. 100640, 2021.
- [13] C. Haro-Pérez, M. Lovallo, L. R. Moreno-Torres, A. Ramirez-Rojas, L. F. Rojas-Ochoa, A. B. Zuccolotto-Bernez, and L. Telesca, “Investigating the time dynamics of photon sequences scattered by tracer particles immersed in a polymeric gel,” EPL (Europhysics Letters), vol. 115, p. 47004, aug 2016.
- [14] F. Schwabl, Statistical Mechanics. 2006.
- [15] B. Chu, Laser Light Scattering: Basic Principles and Practice. 1981.
- [16] G. J. O.-M. C. Haro-Pérez and L. F. Rojas-Ochoa, “Three dimensional cross-correlation dynamic light scattering by non-ergodic turbid media,” J. Chem. Phys., vol. 134, pp. 287–305, may 2011.
- [17] P. R., Dynamic Light Scattering, Applications of Photon Correlation Spectroscopy. 1985.
- [18] G. D. Cohen, Fundamental Problems in Statistical Mechanics II. 1968.
- [19] K. Schätzel, “Rate correlation and data preprocessing with digital correlators and structurators,” In: Schulz-DuBois E.O. (eds) Photon Correlation Techniques in Fluid Mechanics, vol. 38, pp. 226–234, 1983.

- [20] L. Mandel, “Fluctuations of photon beams: The distribution of the photo-electrons,” Proceedings of the Physical Society, vol. 74, pp. 233–243, sep 1959.
- [21] “GitHub, cinvestav-t18.” <https://www.github.com/CINVESTAV-T18/PhotonSTR-18/>. Accessed: 2021-28-01.
- [22] F. F. Molteni M, “Commercial counterboard for 10 ns software correlator for photon and fluorescence correlation spectroscopy,” Rev Sci Instrum, vol. 87, p. 113108, Nov 2016.
- [23] D. Gembris, M. Neeb, M. Gipp, A. Kugel, and R. Männer, “Correlation analysis on gpu systems using nvidia’s cuda,” Journal of Real-Time Image Processing, vol. 6, pp. 275–280, Dec 2011.
- [24] J. B.-J. W. K. J. L. G. Mocsar¹, B. Kreith¹ and G. Vamosi, “Note: Multiplexed multiple-tau auto- and cross-correlators on a single field programmable gate array,” Rev Sci Instrum, vol. 83, p. 046101, April 2012.
- [25] S. K. Abeykoon, M. Lin, and K. K. Van Dam, “Parallelizing x-ray photon correlation spectroscopy software tools using python multiprocessing,” in 2017 New York Scientific Data Summit (NYSDS), pp. 1–10, 2017.
- [26] D. Waithe, M. P. Clausen, E. Sezgin, and C. Eggeling, “FoCuS-point: software for STED fluorescence correlation and time-gated single photon counting,” Bioinformatics, vol. 32, pp. 958–960, 11 2015.
- [27] “National Instruments, graphical programming.” <https://www.ni.com/getting-started/labview-basics/dataflow>. Accessed: 2020-09-01.
- [28] G. Ojeda-Mendoza, A. Moncho-Jordá, P. González-Mozuelos, C. Haro-Pèrez, and L. Rojas-Ochoa, “Evidence of electrostatic-enhanced depletion attraction in the struc-

- tural properties and phase behavior of binary charged colloidal suspensions,” Soft matter, vol. 14, p. 1355—1364, February 2018.
- [29] H. Senff and W. Richtering, “Temperature sensitive microgel suspensions: Colloidal phase behavior and rheology of soft spheres,” J. Chem. Phys., vol. 11, p. 1705, July 1999.
- [30] M. Braibanti, C. Haro-Pérez, M. Quesada-Pérez, L. F. Rojas-Ochoa, and V. Trappe, “Impact of volume transition on the net charge of poly-*n*-isopropyl acrylamide microgels,” Phys. Rev. E, vol. 94, p. 032601, Sep 2016.
- [31] C. Urban and P. Schurtenberger, “Characterization of turbid colloidal suspensions using light scattering techniques combined with cross-correlation methods,” Journal of Colloid and Interface Science, vol. 207, no. 1, pp. 150 – 158, 1998.
- [32] P. Grangier, G. Roger, and A. Aspect, “Experimental evidence for a photon anticorrelation effect on a beam splitter: A new light on single-photon interferences,” Europhysics Letters (EPL), vol. 1, pp. 173–179, feb 1986.
- [33] J. Hloušek, M. Dudka, I. Straka, and M. Ježek, “Accurate detection of arbitrary photon statistics,” Phys. Rev. Lett., vol. 123, p. 153604, Oct 2019.
- [34] R. H. Brown and R. Twiss, “Lxxiv. a new type of interferometer for use in radio astronomy,” The London, Edinburgh, and Dublin Philosophical Magazine and Journal of Science, vol. 45, no. 366, pp. 663–682, 1954.
- [35] X. T. Zou and L. Mandel, “Photon-antibunching and sub-poissonian photon statistics,” Phys. Rev. A, vol. 41, pp. 475–476, Jan 1990.
- [36] H. J. Kimble, M. Dagenais, and L. Mandel, “Photon antibunching in resonance fluorescence,” Phys. Rev. Lett., vol. 39, pp. 691–695, Sep 1977.

- [37] E. M. Purcell, “The question of correlation between photons in coherent light rays,” Nature, vol. 178, pp. 1449–1450, Dec 1956.